

This is a “preproof” accepted article for *Journal of Glaciology*.
This version may be subject to change during the production process.
10.1017/jog.2025.10

Basal reflectance and melt rates across the Ross Ice Shelf, Antarctica, from grounding line to ice shelf front

Daniel Price¹, Joseph Snodgrass¹, Wolfgang Rack¹, Heather Purdie², Christina Hulbe³, Christian T. Wild⁴, Craig Stevens^{5,6}, Oliver J. Marsh⁷, Michelle Ryan¹, Adrian McDonald¹, Kelly Gragg³, Martin Forbes³

¹Gateway Antarctica, School of Earth and Environment, University of Canterbury, Christchurch, New Zealand

²School of Earth and Environment, University of Canterbury, Christchurch, New Zealand

³School of Surveying, University of Otago, Dunedin, New Zealand

⁴Department for Geoscience, University of Tübingen, Tübingen, Germany

⁵Ocean Dynamics Group, New Zealand National Institute of Water and Atmospheric Research, Wellington 6241, New Zealand

⁶Department of Physics, University of Auckland, Auckland 1010, New Zealand

⁷British Antarctic Survey, Cambridge, United Kingdom

Correspondence: olrs@bas.ac.uk

ABSTRACT

We present a 1000 km transect of phase-sensitive radar measurements of ice thickness, basal reflection strength, basal melting, and ice-column deformation across the Ross Ice Shelf (RIS). Measurements were gathered at varying intervals in austral summer between 2015 and 2020, connecting the grounding line with the distant ice shelf front. We identified changing basal reflection strengths revealing a variety of basal conditions influenced by ice flow and by ice-ocean interaction at the ice base. Reflection strength is lower across the central RIS, while strong reflections in the near-front and near-grounding line regions correspond with higher basal melt rates, up to $0.47 \pm 0.02 \text{ m a}^{-1}$ in the north. Melting from atmospherically warmed surface water extends 150-170 km south of the RIS front. Melt rates up to $0.29 \pm 0.03 \text{ m a}^{-1}$ and $0.15 \pm 0.03 \text{ m a}^{-1}$ are observed near the grounding lines of the Whillans and Kamb Ice Stream, respectively. Although troublesome to compare directly, our surface-based observations generally agree with the basal melt pattern provided by satellite-based methods but provide a distinctly smoother pattern. Our work delivers a precise measurement of basal melt rates across the RIS, a rare insight that also provides an early 21st century baseline.

This is an Open Access article, distributed under the terms of the Creative Commons Attribution-NonCommercial-NoDerivatives licence (<http://creativecommons.org/licenses/by-nc-nd/4.0>), which permits non-commercial re-use, distribution, and reproduction in any medium, provided that no alterations are made and the original article is properly cited. The written permission of Cambridge University Press must be obtained prior to any commercial use and/or adaptation of the article.

1. INTRODUCTION

The Antarctic Ice Sheet (AIS) holds 70% of the world's freshwater, which would raise sea-level by 58 m if completely melted (Fretwell and others, 2013; Rignot and others, 2019). Between 1979 and 2017, the AIS contributed 0.014 ± 0.002 m to sea level rise, with a six-fold acceleration in mass loss over those four decades (Rignot and others, 2019). The AIS future contribution to sea level rise has a large uncertainty (Deconto & Pollard, 2016; Seroussi and others, 2023), with low confidence surrounding modelled mass loss and gain processes. Across a range of scenarios, the AIS is expected to contribute between 0.04 m and 0.21 m to eustatic sea level rise by the end of the century (Edwards and others, 2021).

Increases in ice shelf mass loss (Gudmundsson and others, 2019) have likely played a significant role in the observed seaward acceleration of the AIS (Diener and others, 2021). These floating extensions of the grounded ice sheet lose mass via basal melting or iceberg calving. Over the last quarter century, mass loss from basal melting and iceberg calving has been shown to be approximately equal; however, different regions exhibit variability in their contributions from the two processes (Greene et al., 2022). Reduction or collapse of ice shelves can lead to an imbalance of the grounded ice sheets due to loss of ice shelf buttressing (Rott and others, 2002) and resultant thinning and seaward acceleration of grounded ice upstream (Rack & Rott, 2004; Rignot and others, 2004; Dupont & Alley, 2005; Hulbe and others, 2008). Nearly one-fifth of the grounded AIS drains into the Ross Ice Shelf (RIS). The RIS, like the Ronne-Filchner and Amery ice shelves, is a large cold cavity system. Although locally high melt rates are apparent at the ice front and some deep grounding lines, to date, it has not been subjected to significant melting over most of its area (Rignot and others, 2013; Gudmundsson and others, 2019; Rignot and others, 2019; Adusumilli and others, 2020; Smith and others, 2020). This is primarily due to it being protected from interaction with relatively warm water, in contrast to parts of West Antarctica including the Amundsen Sea coastline (Xie and others, 2024). However, given its size and upstream ice sheet catchment, changing ocean conditions on the adjacent continental shelves will have dramatic impacts on the RIS mass balance with global implications (Edwards and others, 2021). It is thus imperative to collect more information on basal melting and the governing ocean conditions both external to, and within, the cavity (Bennetts and others, 2024).

With a total catchment area of over 2 million km², the RIS is downstream of approximately 11.6 m of sea-level equivalent (Tinto and others, 2019; Fig. 1a). Driven by interaction with the circulating ocean beneath, about one fifth of ice shelf mass loss is due to basal melting under the RIS, the rest to iceberg calving (Depoorter and others, 2013). Direct observations of basal melt processes are exceptionally rare and transient as borehole measurements through the ice shelf are logistically difficult and require significant resourcing. From the late 1970s to today, direct observations of the cavity have been made at seven sites across the 487,000 km² RIS area (Jacobs and others, 1979; Arzeno and others, 2014; Begeman and others, 2018; Stewart and others, 2019; Stevens and others, 2020; Washam and others, 2023; Lawrence and others, 2023; Fig. 1). Satellite observations of ice shelf surface elevation provide long-term and ongoing observations of ice shelf change from which basal mass loss may be estimated. Hindering this approach is the requirement for additional input data, including surface accumulation rate, firn processes, satellite-derived strain rates, and the assumption that the ice flow is in steady-state. In the case of cold cavity ice shelves, where melt rates are low, uncertainties in satellite-based melt rates are often larger than the rates themselves, making change detection difficult. Satellite and airborne estimates suggest that the RIS is near balance, with higher basal melt rates near the grounding line of major

outflows and near the calving front, while melting rates over most of the central ice shelf are very low relative to other ice shelves (Rignot and others, 2013; Moholdt and others, 2014; Adusumilli and others, 2020; Das and others, 2020; Paolo and others, 2023). Few surface-based observations are available with which either the spatial pattern or temporal variation of regional basal melting could be validated and where these exist, the focus has been on sites where higher basal melt rates are expected (Marsh and others, 2016; Stewart and others, 2019; Whiteford and others, 2022).

The RIS cavity is separated roughly along its centre flowline into two distinct tectonic regions, distinguished by bathymetry and magnetic anomalies and closely aligned with the contemporary glaciological catchment between the geographic East and West RIS (Mouginot and others, 2017; Tinto and others, 2019). Bathymetry beneath the ice shelf is generally deeper beneath the Western RIS (East Antarctic Ice Sheet side) with a mean depth of 670 m and shallower beneath the Eastern RIS (West Antarctic Ice Sheet side) with a mean depth of 560 m (Tinto and others, 2019). This bathymetry influences the water-column thickness, resulting in a thicker subshelf cavity beneath the Western RIS and thinner cavity beneath the Eastern RIS.

Antarctic ice shelves experience three modes of basal melt driven by ocean circulation (Jacobs and others, 1992). Mode 1 involves the intrusion of dense and salty shelf waters, for the RIS, specifically High Salinity Shelf Water (HSSW) at depth toward the grounding line where melting results in the formation of Ice Shelf Water (ISW). HSSW, or slightly meltwater-modified HSSW has been observed within the cavity both centrally (Stevens and others, 2020), at the southern extremity (Begeman and others, 2018), and on the Siple Coast (Lawrence and others, 2023). Mode 2 is associated with warm waters originating off the continental shelf, specifically modified Circumpolar Deep Water (mCDW). The RIS cavity is currently thought to be sheltered from warmer water masses beyond the distant continental shelf break (Depoorter and others, 2013; Moholdt and others, 2014; Tinto and others, 2019). However, water masses and circulation on the continental shelf are not well-observed in space or in time (Jacobs and Giulivi, 2010; Jendersie and others, 2018). Under present day conditions, ocean circulation models suggest that mCDW inflow into the cavity is possible, primarily in the central sector but penetration is limited (Tinto and others, 2019). This mode has not been observed at any of the RIS borehole sites to date. Mode 3 is a shallow circulation of seasonal warm Antarctic Surface Water (AASW), that drives melting near the ice shelf front (Fig. 1). Observations and modelling indicate that HSSW inflow is mostly confined to the western RIS and that AASW inflows only around Ross Island (Stewart and others, 2019; Tinto and others, 2019).

Non-intrusive geophysical techniques can be used to survey sub-surface features such as internal layers, crevasses and the ice shelf base. Repeated Autonomous phase-sensitive Radio Echo Sounding (ApRES) surveys of the ice column allow the calculation of total thickness change and separation of vertical strain and basal melt rates (Brennan and others, 2014; Nicholls and others, 2015). Across the central RIS, even low magnitude variations in basal mass balance are important for evaluating the mass balance of the ice shelf as a whole, as they potentially occur over extensive areas. Ice shelf-wide surveys on the Filchner-Ronne Ice Shelf (Vaňková and others, 2021; Vaňková and Nicholls 2022) reveal seasonally variable melt regimes influenced by the ocean cavity and sea ice conditions and intermittent basal accretion periods that are not possible to identify with current satellite techniques, but can be important for predicting future mass-balance and stability. More localised investigations there show moderate melt rates (in comparison to warm cavity ice shelves, e.g. Wild and others,

2024) near the southern grounding line and identify the need for the use of recent satellite velocity fields when comparing satellite and surface-based melt rates (Zeising and others, 2022).

Previous ApRES surveys on the RIS have been limited to specific, localised higher melt rate areas. The four previous studies measured basal melt and vertical strain rates at the north-western ice shelf front (Stewart and others, 2019), near the Whillans Ice Stream (WIS) grounding line as part of the Whillans Ice Stream Subglacial Access Research Drilling (WISSARD) project (Marsh and others, 2016; Begeman and others, 2018), and the Kamb Ice Stream (KIS) (Whiteford and others, 2022) grounding line (locations in Fig. 1). Begeman and others (2018) identified low melt rates $< 0.10 \text{ m a}^{-1}$ at the WIS grounding line, maintained by stratification from freshwater injection due to ice melt that persisted throughout the water column and was strongest in the ice shelf boundary layer. In the same region, Marsh and others (2016) used ApRES to examine a basal channel 1.7 km seaward of the WIS grounding line, where they found melt rates up to $16\text{--}22 \text{ m a}^{-1}$ at sites closest to the grounding line. The very high rates were attributed to subglacial lake drainage from beneath the WIS along distinct subglacial channels. Similarly, Whiteford and others (2022) observed a basal melt channel in which very high melt rates, up to 35 m a^{-1} in a narrow $1.5 \text{ km} \times 200 \text{ m}$ zone, have eroded up to 50 % of the total ice thickness. Basal melting rates measured near the calving front adjacent to Ross Island, driven by warm summer AASW, ranged from 7 m a^{-1} near the front to 1 m a^{-1} at the southern end of the survey grid near White Island (Stewart and others, 2019). These localised investigations leave the majority of the ice shelf unexplored.

This study evaluates the spatial and temporal patterns of basal reflection strength, basal melting and strain deformation along a traverse spanning the entire length of the RIS, providing a precise measurement and context for satellite and airborne approaches, and a more spatially comprehensive view than previously available. We make use of multi-annual ApRES measurements collected during repeat heavy vehicle traverses from Scott Base on Ross Island at the northwestern front of the ice shelf to the WIS and KIS grounding lines in the southeast. Along the way, the traverse crosses numerous flow bands of ice with different origins, including glaciers and ice streams, their lateral shear margins and the suture zones between these.

Figure 1 near here

2. ApRES MEASUREMENTS, SURVEY AREA AND METHODS

The ApRES was developed to precisely measure changes of internal and basal reflectors to mm precision in ice up to 2000 m thick (Brennan and others, 2014; Nicholls and others, 2015). Satellite remote sensing approaches infer thickness from freeboard and attempt to approximate the air-snow interface; they must account for snow accumulation and firn compaction rates when interpreting surface elevation change in terms of ice thickness change. Further, satellite-based methods use remotely-sensed horizontal velocity and a steady-state flow assumption to evaluate thinning associated with ice flow. By co-registering geophysical measurements at the firn-ice transition boundary, ApRES approaches are able to exclude snow and firn processes, leaving vertical strain rates and basal mass balance to be quantified. The vertical strain rate of the ice column is measured directly using the relative movement of internal reflectors, and when applied over the ice column thickness, any residual thickness change must be due to basal melting.

The ApRES measurements for this work consist of 32 sites along a 1000 km transect of the United States South Pole Traverse (SPoT) and New Zealand Siple Coast Traverse (SCT) routes (Fig. 1). The record began in the 2015/16 Antarctic field season along the northern section of the SPoT route (Ryan, 2016) from S1 to S12 providing data representative of calendar years 2016 through 2019. In 2018/2019 this was extended to the KIS grounding line across S13-S32 providing data representative of calendar year 2019. This survey was designed to fill gaps between prior measurements, taking advantage of the multiyear logistics support provided by the SCT.

The SPoT route crosses flow bands emerging from Transantarctic Mountain (TAM) valley glaciers and the Mercer and Whillans ice streams. The semi-regular spacing of our ApRES sites (approx. 40 km) reflects a compromise between spatial coverage and traverse driving requirements. Nevertheless, a wide range of flow bands and conditions under the RIS are sampled. The marked sites advect with ice flow in a Lagrangian framework, such that repeat observations sample the same ice column, and thinning rates derived from them represent conditions along a particular segment of each flow band. The SPoT sites S1 to S21 are arranged linearly along the SPoT route covering the majority of ice streams from the East Antarctic Ice Sheet, along the TAMs, south of 78° S. S1 begins on the edge of the Byrd Glacier outflow and continues south to the SCT turn off at S21 (Fig. 1).

The SCT route crosses flow bands from the WIS and KIS. Large folds in streaklines through this region reveal a history of changing flow speed and direction on century time scales (Hulbe and Fahnestock, 2007; Catania and others, 2012). Today, ice flux from WIS is declining (Beem and others, 2014; Winberry and others, 2014; Siegfried and others, 2016) and KIS is stagnant along most of its course with ice discharge into the RIS negligible (Retzlaff and Bentley, 1993; Catania and others, 2006; Rignot and others, 2017). At the same time, the two ice streams' hydrologic systems remain active (Carter and Fricker, 2012; van der Wel and others, 2013; Gustafson and others, 2022) and subglacial meltwater from both systems flows into the RIS ocean cavity as measured by the aforementioned ApRES investigations (Marsh and others, 2016; Whiteford and others, 2022). SCT sites S22 to S27 run across-flow downstream of the WIS grounding line, on either side of the ice plain upstream of the Crary Ice Rise (CIR). Sites S28 to S32 are arranged parallel to flow downstream from the KIS, approaching to within 8 km of the grounding line at S32.

ApRES operates by transmitting a sinusoidal tone (chirp) that sweeps linearly from 200 MHz to 400 MHz over one second. Following this transmission, the reflected signal is received shortly after, consistently exhibiting a frequency lower than the transmitted signal. The standard range resolution for the system is approximately 43 cm, however, the phase of the transmitted wave is also recorded and can be tracked through phase sensitive processing techniques to increase resolution to millimetre precision (Brennan and others, 2014). ApRES precision allows even millimetre changes in absolute ice thickness to be tracked between site visits. By tracking internal reflectors (not layers) across revisits, ApRES data can be used to calculate changes in relative reflector positions in the ice column, from which strain thinning or thickening is inferred. Here, we follow the ApRES phase-coherent processing chain for melt rates and strain, well documented in Nicholls and others (2015) and Brennan and others (2014).

At each site, we collected a series of 20 or 30 discrete radar chirps using the mean for each measurement. To calculate relative internal-layer displacements between two site revisits, we

tracked the phase of the radar signal by cross-correlating 4 m data chunks from the first and second visit. We focused on internal reflectors below the 60 m firn layer, using only those that exhibited greater than 70 % phase coherence in the returned power. The relative internal-layer displacement was unwrapped from the depth within the ice column where the absolute cross-correlation coefficient was highest. This allowed us to calculate absolute internal-layer displacement and apply a linear fit across the ice column to estimate the location of the ice base, assuming deformation due to strain and a minimum of 3 coherent internal layers. The strain rate was determined as the slope of this linear fit, divided by the time span between the revisits. The accuracy of the ice-base displacement estimate was quantified by evaluating the root-mean-square error of the linear fit applied to the absolute internal-layer displacement. The uncertainty bounds of the strain-deformed ice base directly translated into the uncertainty bounds of the calculated melt rate. This is because the ice-base displacement, when compared to the strain-fitted displacement, provides the residual that determines the melt rate. Therefore, any uncertainty in the ice-base offset influences the accuracy of the melt rate estimate.

Basal melt rates were calculated using a MATLAB software processing procedure *fmcw_melt* (see *Data Availability*). Where a basal melt rate could not be constrained, it was not reported, and was likely driven by changes in the waveform around the expected basal reflector so that it could not be matched, and/or too few high correlation values for the linear fit used to calculate the contribution of the vertical strain rate to observed thickness change. The basal melt rate error is the quality of the linear strain fit to the unwrapped internal layer displacement (Brennan and others, 2014; Nicholls and others, 2015). In cases where no clear ice base was visible in the radar return, we still provided a strain-rate estimate based on the internal-layer data if the linear fit criteria were met. We were able to estimate basal melt rate and vertical strain rate across 75 % and 91 % of sites respectively.

Basal reflection strength for each ApRES measurement was interpreted as *strong*, *moderate*, *weak* or *very weak* according to the power of the basal reflection relative to surrounding returns (Fig. 2). A linear fit was applied to the reflection amplitudes near the estimated ice shelf base. The difference between the fit and the peak power was determined as the basal reflection power. *Strong* peaked basal reflections indicate limited scattering from a uniform ice base while *moderate*, *weak* and *very weak* returns likely indicate an additional influence on the radar wave propagation through the ice column or at the base. Typical waveforms for these four classifications are shown in the inset of Fig. 2a. The difference in reflection power is quantified across the ApRES transect in Fig. 2b which defines the reflection strength bounds as provided by the difference between the linear fit and the peak. For additional clarity, specific radargram data examples for each category are provided in the *Supplementary Material* (Figure S1) along with the full list of site reflection values and their associated waveforms (Figure S2). The mean value of the resultant power differences at each site were categorised following: *strong* ≥ 35 dB, *moderate* ≥ 25 dB and < 35 dB, *weak* < 25 dB and ≥ 10 dB and *very weak* < 10 dB. In some cases for *very weak* returns, it was necessary to use other years to guide the application of the linear fit across the estimated basal range to provide an estimate of basal power differences (see Figure S1).

The ice thickness at each site was calculated using a constant radar wave velocity of 0.169 m ns^{-1} to determine the range of the basal reflector from the two-way travel time. Across sites classified as *strong* and *moderate* the *fmcw_melt* procedure automatically determined ice thickness which could be manually confirmed on the x-axis of the resultant radargram as the range with the highest power return. If the reflector was ambiguous as determined by the

software, we manually selected the thickness which was determined using the strongest reflector within the expected basal range. At certain sites this was difficult to achieve, particularly with *very weak* returns. We qualitatively used multiple years to guide the estimation of thickness at these sites. A radar firm correction was then applied to the raw ice thicknesses to account for increased radar wave velocity in the lower density firn (Ligtenberg and others, 2011; Ryan, 2016). A spatially variable radar thickness correction was applied across the ApRES transect using the firn air content provided by Morlighem (2022). We did not consider firn air content variability through time because of advection.

3. RESULTS

3.1 Ice thickness

Ice shelf thickness from the 2019 ApRES measurements is displayed in Table 1, along with the difference from thickness in the Bedmap2 (Fretwell and others, 2013) and BedMachine V3 (Morlighem and others, 2020; Morlighem, 2022) datasets. The highest ice thicknesses measured across the survey are upstream of the CIR, with a maximum of 695.6 m, 4 km from the grounding line at S24. The thinnest ice was identified in the central ice shelf between S10 and S13 with a minimum of 317.9 m at S13. Satellite-derived thickness align with these areas of minima and maxima and produce the same pattern of thickness along the ApRES transect. In general, our ApRES-derived thicknesses are greater than altimetry-based estimates. Exceptions to this are found across the central ice shelf from S10 to S13 an area characterised by *weak* basal reflections.

3.2 Reflection strength

The basal reflection strengths broadly produce a pattern of *strong* reflectors in the north nearer to the calving front, reduced but variable in the central region, returning to *strong* again to the south near the grounding lines. Sites S1 to S3 are characterised by *strong* basal reflections. Between S4 and S20 varying reflection strengths are recorded with an intermittent pattern. Returns are *weak* at S5 and S6, from S10 to S13, the area surrounding the HWD2 borehole and at S19 and S20. To the south of S21, reflections return to *strong* and remain so until S27 which is measured as *weak*. The remaining sites approaching the KIS grounding line are all *strong* except S29 with a *moderate* return. The general pattern identified by the ApRES reflection strengths compares well with similar classifications provided by airborne radar surveys in the 1970s (Neal, 1979; Fig. 2a) and mid-2010s (Tinto and others, 2019; Fig. 2c). Both airborne data sets identify distinct areas of strong basal reflectivity in the north and a variable and lower reflectivity in the central ice shelf. This again increases to the south around S21-S24.

3.3 Basal melt rates

Basal melt rates were resolved at 24 of the 32 sites (Table 1 and Fig. 3). The mean basal melt rate across the whole transect is $0.094 \pm 0.013 \text{ m a}^{-1}$. This RIS-wide ApRES melt signal is characterised by significant regional variability (Fig. 3a; Fig. 3f). From the magnitude of melt rate and basal reflection strength, the RIS transect can be classified into five zones with different basal melting regimes referred to as (1) Siple High Melt Zone (Siple-HMZ), (2) Southern Low Melt Zone (Southern-LMZ), (3) Southern High Melt Zone (Southern-HMZ) (4) Central Low Melt Zone (Central-LMZ) and (5) Northern High Melt Zone (Northern-HMZ) (shown in Fig. 3a). High and low melt zones are split above and below the mean

transect basal melt rate of 0.094 m a^{-1} identified by this study. Below we provide results starting from the southern end of the ApRES transect and move northward.

The Siple-HMZ is occupied by only one site; S32 has a melt rate of 0.145 m a^{-1} - above the RIS mean basal melt rate. The classification of this area with a relatively high melt rate is supported by other work which is referred to in Section 4.3.1. Moving away from the KIS grounding line, sites S31 to S28 run near-perpendicular to the KIS grounding line and form the KIS component of the Southern-LMZ. Here, the melt rate declined rapidly, from $0.145 \pm 0.011 \text{ m a}^{-1}$ at S32 to $0.040 \pm 0.003 \text{ m a}^{-1}$ just 14 km downstream, to $0.009 \pm 0.003 \text{ m a}^{-1}$ at S28. Across the KIS-WIS suture zone to the southwest, sites S27 to S25 occupy ice with origin in the WIS between the KIS and CIR. These sites have low melt rates close to zero, the mean melt rate for the Southern-LMZ is 0.027 m a^{-1} .

Moving away from the grounding line at S24, now on the southwestern side of the CIR but still on ice with origin in the WIS, melt rates begin to rapidly increase. Melt rates are two orders of magnitude larger than those to the northeast in the Southern-LMZ (0.002 m a^{-1} at S27 and 0.285 m a^{-1} at S21, Table 1; Fig. 3a). This increase marks a transition to the Southern-HMZ (S23-20). The pattern of higher melt rate toward the grounding line reverses in the Southern-HMZ, where lower melt rates are observed closer to the grounding line, so much so that S24 ($0.090 \pm 0.007 \text{ m a}^{-1}$) dropped below the transect mean and was designated as a low melt site. Higher rates, reaching a maximum of $0.285 \pm 0.034 \text{ m a}^{-1}$ at S21 are observed between CIR and the TAM coastline.

Across the Central-LMZ (S4 to S19) it was only possible to measure melt rates at 8 of 16 sites (Table 1; Fig. 3f). At 6 of the 8 sites identified with *weak* basal reflection strengths (S5, S6, S10 to S13) melt rates could not be estimated. At S15 and S16 which returned *strong* and *moderate* reflections respectively, melt rates were also not measurable as vertical strain was not determined. The maximum detected melt rates were $0.024 \pm 0.012 \text{ m a}^{-1}$ and $0.024 \pm 0.002 \text{ m a}^{-1}$ at sites S8 and S18, respectively, values three to four times lower than the minimum measured values in the higher melt rate zones to the north and south. The mean basal melt rate across the Central-LMZ was $0.014 \pm 0.021 \text{ m a}^{-1}$. Negative rates were measured at S17 and S19.

Satellite and airborne derived basal melt rates provided by other analyses are included in Fig. 3b for comparison. Their ice shelf-wide data is presented for context in Fig. 3c-e. For all datasets we retrieved the spatially coincident mean basal melt rate value at the ApRES 2019 site positions. We use datasets provided by Paolo and others (2023), Adusumilli and others (2020), and Das and others (2020) herein referred to as P2023, A2020, and D2020 respectively. The spatial patterns identified by the various approaches are similar, however the range of melt rates obtained using ApRES is smaller than in the other cases from 1.20 m a^{-1} to -0.67 m a^{-1} in P2023, 1.22 m a^{-1} to -0.53 m a^{-1} in D2020, and 0.49 m a^{-1} to -0.53 m a^{-1} in A2020. We provide more detailed discussion of the differences between these datasets and the ApRES survey in Section 4.3.6.

Table 1 near here

Figure 2 near here

Figure 3 near here.

Repeat surveys over five consecutive years in the Northern-HMZ (S1 to S3) allow interannual variability to be assessed across varying intervals (Fig. 4a). The pattern of higher melt rate closer to the ice shelf margin is consistent across years and connects well with other observations made closer to the front (Fig. 4b; Stewart and others, 2019). The largest interannual differences are also observed closer to the front. The highest melt rates of the survey were measured in this zone; S1 and S2 recorded mean melt rates of $0.468 \pm 0.020 \text{ m a}^{-1}$ and $0.328 \pm 0.013 \text{ m a}^{-1}$ respectively. To the south, around S3, ~ 170 km from the ice shelf front, melt rates return to the RIS-wide average.

A two-year measurement period between November 2017 and January 2020 was calculated alongside available one-year repeats. Highest melting was observed through 2017 and the lowest through 2016 across S1 and S2, 2018 and 2019 melt rates were between those measured in 2017 and 2016. The mean melt rate of all available measurements at each site is shown and extended northward to near the ice shelf front (Fig. 4b) with data from Stewart (2018).

Figure 4 near here.

3.4 Vertical strain rates

Over most of its area, the ice shelf experiences dynamic thinning as its velocity increases seaward, except where obstructions like ice rises can create compression and thickening. In some areas, most notably downstream of WIS, KIS, and Byrd Glacier, the flow of the ice shelf is not at steady state due to past and ongoing variations in ice stream and glacier discharge into the shelf (Hulbe & Fahenstock, 2005; Campbell and others, 2018; Das and others, 2020). Thickening, a positive vertical strain, was only observed at S24, upstream of CIR and south of the CIR grounding line (Table 1, Fig. 3a). None of the errors are greater than the strain magnitude at any site. Vertical strain could not be calculated at three sites in the central RIS (S13, S15, and S16) due to sub-threshold correlation coefficients of internal layers between measurements, such that the minimum number of internal matches required to fit the linear model could not be achieved (see Section 2).

Our surface-based measurements of vertical strain rate agree well (Fig. 5), in general, with estimates made using the satellite-based Making Earth System data records for Use in Research Environments (MEaSURES) velocity (Rignot and others, 2017) following Alley and others (2018). Notable differences were found along the flanks of CIR, particularly at S21, S25, and S26 where ApRES found thinning, while the satellite-velocity approach yields thickening. At all other sites the sign is the same. At S18, slightly downstream and northwest of CIR, the thinning rate implied by the MEaSURES velocities is twice the rate we measure. At S22 it is nearly four times the ApRES-measured value.

Figure 5 near here.

4. DISCUSSION

4.1 Ice Shelf Thickness

The general pattern of our ApRES-derived ice thickness transect follows ice thickness estimates using satellite altimetry across the RIS. ApRES-derived thickness is typically higher, with the exception of sites characterised by weaker basal reflection strengths across the Central-LMZ (Table 1, Fig. 2). Across these sites (S10 to S13) the Bedmap2 mean thickness is 22.9 m thicker, and the BedMachine V3 is 4.0 m thicker. It is impossible to conclude with confidence the reason for the discrepancy in thicknesses across this area. One hypothesis is that the ApRES identifies a reflector that is not the true ice base resulting in an underestimate of thickness. In support of this, at site S12, a sharp interface between bubbly glacier ice and bubble-poor ice containing sediment was observed via borehole at about 60 m from the ice base (Stevens and others, 2020). The ApRES basal reflection is *weak* at this site making it difficult to pick the basal reflection with confidence. Our derived thickness estimate at this site is about 40 m thinner than the thickness implied by water pressure measured at the base of the borehole (Table 1 – S12). Together, these observations suggest a deep internal reflector of the type usually associated with a basal marine ice layer (see for example, Fricker and others, 2001). This is discussed further below related to reflection strengths in this area.

4.2 Reflection Strength

The ApRES reflection depends on properties and property contrasts within the ice column and the morphology of the ice base. Sounding characteristics at individual sites must thus reflect upstream origins and ocean interactions of the ice at each location. The transect crosses numerous flow bands, each with its own ice flow history, providing an opportunity to examine how this source of heterogeneity in the ice affects the ApRES observations (Fig. 1, Fig. 6, Table 1).

Strong basal reflections indicate a simple interface and a high dielectric contrast. These conditions are interpreted to indicate minimal roughness, and a strong dielectric contrast maintained by basal melting. Along the transect, *strong* basal reflections are associated with sites near the ice shelf front and with larger flux outlet glaciers and ice streams (Fig. 1; Fig. 2a). Sites close to the KIS and WIS grounding lines are also characterised by *strong* basal reflections. Melt rates at these sites vary across two orders of magnitude (Table 1), including some of the lowest melt rates observed. The basal melting responsible for a sharp basal contrast may reflect conditions experienced upstream of, rather than at, the observation site. The overall low rates of melting and freezing under cold-cavity conditions, allow for basal features to remain relatively unmodified long after their formation somewhere upstream.

All sites southeast of CIR across the WIS and KIS outflows (S25-S32) have *strong* returns except for S27 and S29. Basal crevassing is identified in the vicinity of the KIS grounding line (MacGregor and others, 2017) and could be present across the wider region. Our results indicate that at S29 basal crevasses could be present. Basal crevassing influences the strength of the basal return causing an additional peak in the power return ahead of the actual ice base (Zeising and others, 2024; their Fig. A1 and A2). We see a similar return at S29 (see

Supplementary Material Fig. S2cc) which indicates an off-nadir reflection, potentially from a basal crevasse. A similar less pronounced peak is also present in the waveform at Directly upstream of S27 (Fig. S2aa). In addition, so the southeast of S27, Neal (1979) identified an area of lower reflectivity which provides further evidence of an ice column that is lowering the radar reflectivity along this flowline. These two influences would account for the *weak* reflection strength amongst the dominant *strong* reflectors across the region. Ground penetrating radar surveys spatially coincident with the ApRES measurements would help confirm these assumptions. Lower basal reflection strengths can also be associated with some shear margins and sutured zones between outlet glaciers, and ice with a complicated deformation history, for example, S19 and S20 where the ice has origins in the true left margin of the Mercer Ice Stream. Ice in these flow bands has experienced relatively large deformation rates (LeDoux and others, 2017).

Weak and *very weak* classifications indicate a diffuse reflector. Conductivity contrasts due to impurities in the ice column, and ice crystals accreting at site or upstream could all contribute to this individually or collectively. In the RIS, *weak* and *very weak* reflections are observed in shear margin flow bands, including one with basal melt channels near the grounding line (Table 1). The locations of *weak* and *very weak* reflections match well with the general distribution of weaker airborne radar reflections observed more than 40 years ago by Neal (1979) and more recently during the ROSETTA-Ice survey (Tinto and others, 2019). Borehole observations at S12 revealed a ~60 m thick basal layer of bubble-free ice containing terrestrial sediments. This thick basal layer, likely of marine origin, prevented the ice base from being identified by ApRES causing an underestimate of thickness, a *weak* reflection, and no basal melt signal. By tracing flow lines upstream this ice has origins at the Liv Glacier (white streaklines lines in Fig. 1). ISW and a thin layer of new ice crystals at the ice-ocean interface were also identified at this site (Stevens and others. 2020) and could be playing a role at other Central-LMZ sites. Indeed, variability between repeat measurement reflection strengths could be due to transient conditions at the ice-ocean interface, alternating between the formation and melting of marine ice crystals due to temporal variations in cavity circulation. Together, our observations suggest caution in how such change is interpreted and that further investigation is warranted, ideally via a longer-term time-series assessment at a temporal resolution that can capture these sporadic events.

Figure 6 near here.

4.3 Basal Melt Rates

The mean melt rate across our sites, $0.094 \pm 0.013 \text{ m a}^{-1}$, agrees well with other shelf-wide estimates, well within the range of satellite-based average rates (from 0.07 to 0.11 m a^{-1} ; Rignot and others, 2013; Depoorter and others, 2013; Moholdt and others, 2014). Our observations span a wide range of conditions within the ice shelf cavity (Jendersie and others, 2018) and along with comparisons at individual sites, this outcome provides some surface-based validation for techniques that rely on different assumptions and model-derived inputs. The spatial pattern of observed melt, that is, increases in melt rate toward the ice shelf front and grounding lines and decreases across the interior is in general agreement with previous work (e.g. Stewart and others, 2019; and satellite analysis, Fig. 3c-e) and with models of ocean circulation, melting and freezing in the ice-shelf cavity (Jendersie and others, 2018).

4.3.1 Kamb High Melt Zone

North of this zone melt rates increase as the ApRES transect approaches the grounding line of KIS, reaching a maximum of 0.145 m a^{-1} at S32. Although the classification of this zone is driven by one site, other work is supportive. Summer ApRES melt rates observed 4 km upstream from S32 (4 km from the KIS grounding line) were $0.1\text{--}0.2 \text{ m a}^{-1}$ and exceeded 1 m a^{-1} at the grounding line (H. Horgan, *pers. comm.*). This compares reasonably with estimated melt rates from a remotely operated vehicle of 0.26 m a^{-1} (Lawrence and others, 2023). These locally high melt rates may be due to heat carried to the grounding line by HSSW or to processes associated with glacial meltwater flowing into the cavity (Whiteford and others, 2022). Begeman and others (2018) and Lawrence and others (2023) identified slightly meltwater-modified HSSW near the WIS and KIS grounding lines, respectively. Together, these observations demonstrate that more work is required to understand heat transport pathways in the RIS cavity as a whole, and to the grounding line in particular. This is especially true regarding connections between the east and west sectors of the cavity which are likely controlled by quite small-scale bathymetric pathways (Tankersley and others, 2022; Tinto and others, 2019).

4.3.2 Southern Low Melt Zone

The pattern of overall low melt rates across the region, is broadly in line with expectation deep within a cold-cavity environment (Jacobs and others, 1979) and in combination with relatively shallow ice including at the grounding line (compared to Ronne or Amery that have higher melt rates deeper despite cold conditions). Models predict a broad region of near-zero or overall slow freezing in this region and limited intrusion of HSSW due to the relatively shallow sea floor in the eastern sector of the ice shelf (Jendersie and others, 2018). A layer of accreted marine ice was observed via borehole at J9, about 90 km downstream of our sites (Fig. 1; Zotikov and others, 1980).

4.3.3 Southern High Melt Zone

This zone is a remote region with few surface-based measurements. Sites S20 to S23 are located on ice that is laterally constrained between CIR and the TAM coastline. Melt rates are high from S23 to S21 but rapidly decrease to the north and east. Shallowing of the ice shelf base, which causes the pressure-dependent melt temperature to rise, may explain the declining melt rate north of CIR. Approaching the grounding line between S23 and S24, melt rates more than halve. Here, the cavity is likely to be narrowing as the ice thickness increases and the grounding line approaches. As discovered by Begeman and others (2018), this may restrict mixing, and a meltwater-derived basal boundary layer could be protecting the base of the ice shelf and contributing to the declining melt rate.

4.3.4 Central Low Melt Zone

Weak internal layer correlations and diffuse basal reflection prevented basal melting from being quantified across much of the central RIS. To the north and south, *moderate* and *strong* returns are also observed, so that overall, the region is characterised by the greatest spatial variability in ApRES radar return characteristics. Spatial variations in ice characteristics due to the numerous flow bands from TAM glaciers, their shear margins, and suture zones can explain some, but not all, of this variability. As discussed earlier, spatial variation in basal melting and freezing must also be important, both upstream of and at the site of each ApRES observation.

While internal layers could still be used to interpret the strain thinning at these sites, the weak basal reflection signature prevented the identification of basal changes required to calculate melt rates. With the thick basal layer identified at S12, and ephemeral accretion of marine ice at site supported by oceanographic data collected at HWD2 (Stevens and others, 2020), it is impossible to confidently constrain the drivers of basal melt values across the Central-LMZ with the available data. The ApRES measurements across this zone support the current understanding that very low basal melt rates dominate the central RIS and that perhaps (only with the support of observations at HWD2) that basal freezing can intermittently occur. Further evidence of a changing basal reflector is provided across sites S4 to S6, S8 to S11, and S15 and S16 (Fig. 2b; Fig. S2). Another source of the varying radargrams between years at these sites could be attributed to inadequate operation (e.g. poorly connected cables, misalignment of antennas) or, a faulty instrument. All steps were taken to avoid such interference; the system was deployed on a sled (removing the need to continuously detach cables), and system tests were completed regularly. In the southern extremity of the zone, the negative sign at S17 and S19 could indicate a switch to basal refreezing with melt rate values of $-0.042 \pm 0.012 \text{ m a}^{-1}$ and $-0.017 \pm 0.056 \text{ m a}^{-1}$ respectively. At S19, a large error indicates significant uncertainty about the basal mass balance sign. We aim to investigate this further at likely accretion sites, following a similar approach to Vaňková and others (2021) once more data becomes available from future ApRES deployments.

4.3.5 Northern High Melt Zone

Under the north-western RIS, Stewart and others (2019) report a strong seasonal melt signal with a large component of the net ablation occurring in summer. The rates are high in comparison to the ice shelf as a whole, their interpolated measurement area represents 20% of the net basal mass loss from the RIS over only 1.6% of its area (Rignot and others, 2013; Stewart and others, 2019). This melt is driven by the seasonal influx of AASW, the influence of which decays to the south as the water cools upon interaction with the ice shelf base (Malyarenko and others, 2019). It is suggested that the strength and duration of the inflow would result in the ventilation of the outer ~ 50-160 km of the cavity. The southernmost measurement sites in Stewart and others (2019) are ~ 80 km from the contemporary ice shelf front and our survey extends these observations to the south with S3 ~ 175 km from the ice shelf front. Our observations confirm the speculation in Stewart and others (2019) and modelling in Tinto and others (2019) that AASW intrusion reaches as far south as Minna Bluff adjacent to S2 ~150 km from the ice shelf front; south of S3, ~170 km from the front, melt rates have returned to the RIS average (Fig. 4b). Therefore, the region between S2 and S3, around 78.82°S likely represents the southernmost influence of present-day Mode 3 melting under the RIS.

Interannual variation in melt could be assessed in the Northern-HMZ. At S1 and S2 the highest melt signal is observed in 2017 and the lowest in 2016 (Fig.4a). Basal melting nearly doubled at each site between the two years, suggesting that the influence of Mode 3 melting was distinctly different in each year. Parkinson (2019) reports prominent negative monthly deviations in sea ice extent in the Ross Sea during 2017, while in 2016 sea ice extent is higher. Further evidence is provided by Brett and others (2020), who observed a similar correlation between both fast ice extent and sub-ice platelet layer thickness in McMurdo Sound and the Ross Sea Polynya activity. This significant variation in sea ice cover, potentially affecting the amount of solar energy absorbed by near-surface waters, may have contributed to the observed differences in ice shelf basal melting between years. A more

detailed analysis of surface waters near the ice shelf front is needed to confidently identify melt rate drivers. Future research into the relationship between sea ice concentration, AASW, and ice shelf basal melt rates will require extended oceanographic observations in parallel with a regional ApRES network.

4.3.6 Satellite & Airborne Comparisons with ApRES

The airborne and satellite datasets with which we compare our ApRES data span a range of timeframes and are presented as area-averaged values, as opposed to the ApRES point measurements (Table 2). Nevertheless, the ability to compare precise melt rate information to relatively coarse satellite and airborne-derived estimates is valuable. The observed differences between ApRES measurements and satellite measurements may be related to this spatial averaging. In some specific cases this may be the cause of large differences, for instance very close to the grounding line where melt can vary by orders of magnitude over as little as 1 km (Marsh et al., 2016).

Both melt and surface accumulation are known to vary on interannual timeframes, so additional differences may be introduced by temporal averaging over different timescales. Errors in the auxiliary products used, for example surface mass balance (SMB) and satellite-derived strain rate will cause further discrepancies. Uncertainties can be introduced in satellite products when thickness differencing occurs on a Eulerian reference frame, due to advection of ice of a different thickness through the fixed observation point.

ApRES measures basal melt in a Lagrangian reference frame and both CryoSat-2 derived A2020 and airborne radar derived D2020 employ the same approach. P2023 use an Eulerian reference frame, with basal melt available on a 3 km grid covering a much longer timespan from 1992 to 2017 (Table 2). P2023 uses ERS, Envisat, and CryoSat-2 altimetry. A2020 and P2023 use different velocity products, and different inputs for their SMB and firn-densification processes (Table 2). D2020 use a Lagrangian reference system to compare the proportions of meteoric ice that are accumulated locally and advected from the continent measured using airborne radar. By integrating these proportions with a satellite-derived velocity and an ice flow model, they derive the surface mass balance and basal melt rates along radar transects. For D2020, we produced melt rates as shown in Fig. 3e using a bivariate spline provided on a ~ 10 km grid.

Overall, D2020 estimates follow the melt rate trends across the ApRES transect, but notable exceptions are identified at S2, and at S20. At S2, D2020 measure an increase in melt rate from S1. This is at odds with all other techniques and the expectation of a decreasing Mode 3 melt influence moving away from the ice shelf front. Given the timespan difference between assessments for D2020 (~ 20 years in this area), and the poorly understood temporal variability of Mode 3 melting under the RIS, it is very possible that a different behaviour may have existed outside of our ApRES window. This is supported by the notable interannual variability in melt rate observed across S1 and S2 even through the short timeframe of this ApRES assessment. From S5 to S7 D2020 measure positive melt rates while other approaches are near zero or negative. At S20 a 0.5 m a^{-1} decrease in basal melt rate is measured. This shift to negative basal melt is also produced by P2023.

P2023 follows the expected trends and ApRES measurements from S1 to S20. From S21 to S23, P2023 shows an extensive range of basal melt estimates, from -0.68 m a^{-1} to 1.2 m a^{-1} far beyond the minimum and maximum measured by ApRES anywhere on the transect. This

trend is also in the opposite direction to ApRES across this area. From S23 to S24, P2023, A2020 and ApRES identify a decrease in melting towards the grounding line. At S25 and S26 melt rates approach 1.2 m a^{-1} in what ApRES identifies as a low melt zone. It is possible that the larger grid size (3 km) allows small areas of high or low melt to skew the mean, or that the effect of advecting topography produces erroneous melt estimates in the P2023 data. We postulate that the complex and locally variable surface topography changes over the satellite era around the CIR and on the WIS to the south could be playing a role in observed discrepancies between ApRES and P2023 (Smith and others, 2020; Verboncoeur and others, 2024). It is also of interest that for our analysis of vertical strain (Fig. 5), satellite-derived strain rates at S21, S25 and S26 (and S23 within its measured standard deviation) are positive, while ApRES vertical strain is negative. These sites are the P2023 values that exhibit the largest deviations from ApRES measured melt rates across this section. At S22 and S24, between these sites on the transect, ApRES and satellite-derived strain are of the same sign and basal melt rates between ApRES and P2023 are remarkably similar. From S28, approaching the KIS grounding line, P2023 derived melt rates return to the more modest ApRES estimates but remain negative until reaching zero at S32. ApRES-derived strain and satellite strain agree well across this area so deviations here could be due to error in the SMB.

A2020 has the most comparable timespan (2010–2018) to the ApRES (2015–2020), although interannual variability may again make a direct comparison difficult. Melt rates follow the expected decreasing trend from S1 to S4 although much lower at S2 and transitioning to a negative melt rate from S3 to S6. From here the melt rate increases, returning to rates comparable to S1, staying positive and above all other methods until S16. This higher melt rate is at odds with the general understanding of negligible melt across the central shelf and in disagreement with the other studies compared here. After differencing the SMB models provided by A2020 and P2023, a slight positive bias is observed in A2020's SMB across this section of the ice shelf; however, this bias is minor and cannot be the sole factor contributing to higher melt rate estimates. Like the variability discussed in P2023 above, this again points toward the treatment of vertical strain rate as derived from the satellite velocity products as the principal source of error. The spatial variability of accumulation rate remains an important factor for satellite observed basal melting estimates with a significant paucity of in situ data. This work originally planned to collect snow accumulation information across the RIS, but this could not be completed for logistical reasons. A 13-month accumulation time series was collected between December 2018 and January 2020 across the SCT (S22 to S32) at 5 km intervals. These data identified a mean accumulation rate of $32 \pm 8 \text{ cm a}^{-1}$ with a slight increase from east to west at a rate of approximately 1 cm per 5 km.

Table 2 near here.

4.4 Vertical Strain Rates

ApRES vertical strain rates have been directly compared to strain rates derived using satellite data (Rignot and others, 2017; Alley and others, 2018). Apart from some variation in the southern areas, ApRES strain rates are in good agreement with satellite strain rates. We noted a significant difference at S18 and S22 (Fig. 5). At S18, the satellite velocity measurement was on the border of two separate satellite acquisition areas, which may have overestimated the strain thinning. Satellite-derived strain methods may struggle around the complex grounding zone around the CIR, where we also note errors in sign between the ApRES and

satellite approaches. This may help explain some of the variation in basal melt estimates between methods across this area. In general, the good correlation between satellite derived strain rates and surface-based ApRES measurements gives greater confidence in the accuracy of other satellite studies of vertical strain and basal melting away from complicated ice dynamics. This study only looked at deformation below the firn transition boundary. A future study of ApRES measurements to include the firn compaction rates acting alongside the strain thinning in the upper layers would provide additional validation.

5. CONCLUSION

This work provides the first ApRES assessment of the Ross Ice Shelf from grounding line to the ice shelf front, revealing a spatially complex distribution of basal reflection patterns, influenced by circulation and water properties in the ocean cavity, and glacial processes upstream of the grounding line. The observations provide an independent check of satellite-based assessments and allow us to consider sources of spatial variation in vertical strain rates and basal melting. Key conclusions are described under three categories:

1. **Basal reflection:** Regions in the north and south of the ice shelf generally exhibited strong basal reflectors indicative of a uniform ice shelf base, likely in a basal melting regime under the influence of Antarctic Surface Water near the ice shelf front, or High Salinity Shelf Water near the grounding lines. Former shear margins, suture zones and basal crevassing are in most cases associated with *moderate* returns. Across the centre of the ice shelf significantly different basal conditions are identified, with radar reflections ranging from *strong* to *very weak*. In one location we observed *weak* reflections and a peak reflection strength shallower than the true ice base (constrained via a borehole). Direct observation via borehole shows the site to be underplated by terrestrial-origin basal ice with marine ice and sediment accreted upstream of the survey site. This suggests that the glaciological context should also be considered when interpreting such signals as indicative of local *marine* ice accretion. This highlights a limitation for the use of ApRES where deep ice contains impurities. Short-lived marine ice accretion events at site, noted in other studies of the central ice shelf, cannot be ruled out as potential influences on ApRES basal reflection strength.
2. **Basal melt rate:** The mean melt rate of $0.094 \pm 0.013 \text{ m a}^{-1}$ across the entire survey transect falls centrally amongst other estimates for the entire RIS. Where measurable, we find very low rates of basal melting across the western RIS interior with two out of the three compared remote sensing datasets reaching the same conclusion. From the central ice shelf, basal melting increased in magnitude to the north, from approximately zero to a maximum of 0.468 m a^{-1} . The southern limit of this northern melt zone is 150-170 km from the ice shelf front. This approximates the contemporary southern limit of Antarctic Surface Water penetration and subsequent Mode 3 melting under the Ross Ice Shelf. Moving south from the ice shelf centre, melt rates increased to 0.285 m a^{-1} along the South Pole Traverse Route to the southwest of Crary Ice Rise. Basal melt rates of $0.01\text{-}0.04 \text{ m a}^{-1}$ were typically observed across the Siple Coast, with an order of magnitude higher rate of 0.145 m a^{-1} observed 8 km from the Kamb Ice Stream grounding zone. The higher rate is not predicted by ocean circulation models and likely points to the presence of High Salinity Shelf Water near the grounding line, consistent with prior ocean observations which identified slightly meltwater-modified High Salinity Shelf Water. Satellite and airborne estimates of basal melt generally followed the same north-south spatial trend as the ApRES rates,

though there were notable differences in the southernmost and central part of the transect. It is likely that erroneous satellite-derived vertical strain in regions of more complicated ice dynamics is causing these discrepancies, while in other regions inaccurate surface mass balance is playing a role.

3. **Vertical Strain:** ApRES vertical strain rates are broadly consistent with satellite-derived strain rates, though significant differences, including sign differences are identified in regions with more complex ice dynamics. These are likely responsible for poor basal melt rate estimates in these regions.

This dataset of ApRES measurements provides a useful guide for planning future research efforts to constrain ice shelf basal properties and basal melt for the Ross Ice Shelf, while capturing a precise early 21st Century reference for basal melt rates.

AUTHOR CONTRIBUTIONS

DP and JS wrote the manuscript with contributions from all authors, while WR and DP conceived the investigation. 2015/16, 2016/17 ApRES surveys were completed by MR and WR, in 2017/18 by AM, KG, MF, in 2017/18 DP extended and carried out the full Ross Ice Shelf transect of ApRES survey and repeated this in 2019/20. JS and DP completed the data analysis, and produced the figures with assistance from CH, CS & CW.

SUPPLEMENTARY MATERIAL

The supplementary material for this article can be found at [*To be provided by journal*]

ACKNOWLEDGEMENTS

The authors would like to thank Antarctic New Zealand for the logistical support to complete the five seasons of ApRES surveys, in particularly members of the New Zealand Siple Coast Traverse team for seasons 2017/18 through 2020/21, Richie Hunter, Geoff Dickey, Robin (Bruce) Davies, Rob Teasdale, Kimbra Hughes, Tim Parkin, Cole Rassmussen, Jason Watson, Kate McKenzie, James Horan, Johnno Leitch & Lawrence Keys who collectively assisted hundreds of ApRES deployments. This research was supported by the New Zealand Antarctic Research Institute funded Aotearoa New Zealand Ross Ice Shelf Programme, the New Zealand Antarctic Science Platform provided support through contract ANTA1801, and the Victoria University of Wellington Hot Water Drilling initiative. We thank the two anonymous reviewers and Editor, Matt Siegfried for their detailed comments and suggestions that significantly improved the quality of the manuscript.

DATA AVAILABILITY

The ApRES raw data, data overview tables, the temporal distribution of ApRES measurements, and the Siple Coast snow accumulation data are available at [https://figshare.com/projects/Ross_Ice_Shelf_ApRES/206932]. MATLAB scripts were kindly provided by Keith Nicholls (British Antarctic Survey) and are available at [https://github.com/ldeo-glaciology/phase-sensitive-radar-processing/tree/main/code/Matlab_fmfw_2018_case_update/revisit]. Airborne radar data from the ROSETTA-Ice program are available at [<https://pgg.ldeo.columbia.edu/data/rosetta->

ice]. All additional data displayed from other studies are available through their associated references.

REFERENCES

Adusumilli S, Fricker HA, Medley B, Padman L and Siegfried MR (2020) Interannual variations in meltwater input to the Southern Ocean from Antarctic ice shelves. *Nature Geoscience.*, **13**(9), 616-620 (<https://doi.org/10.1038/s41561-020-0616-z>)

Alley KE, Scambos TA, Anderson RS, Rajaram H, Pope A and Haran TM (2018) Continent-wide estimates of Antarctic strain rates from Landsat 8-derived velocity grids. *Journal of Glaciology.*, **64**(244), 321-332 (<https://doi.org/10.1017/jog.2018.23>)

Arzeno IB, Beardsley RC, Limeburner R, Owens B, Padman L, Springer SR, Stewart CL and Williams MJM (2014) Ocean variability contributing to basal melt rate near the ice front of Ross Ice Shelf, Antarctica. *J. Geophys. Res. Oceans.*, **119**, 4214–4233 ([doi:10.1002/2014JC009792](https://doi.org/10.1002/2014JC009792))

Beem LH, Tulaczyk SM, King MA, Bougamont M, Fricker HA, and Christoffersen P (2014) Variable deceleration of Whillans Ice Stream, West Antarctica. *J. Geophys. Res. Earth Surf.*, **119**, 212–224 ([doi:10.1002/2013JF002958](https://doi.org/10.1002/2013JF002958))

Begeman CB and 9 others (2018) Ocean Stratification and Low Melt Rates at the Ross Ice Shelf Grounding Zone. *J. Geophys. Res. Oceans.*, **123**(10), 7438–7452 (<https://doi.org/10.1029/2018JC013987>)

Bennetts LG and 37 others (2024) Closing the loops on Southern Ocean dynamics: From the circumpolar current to ice shelves and from bottom mixing to surface waves. *Reviews of Geophysics.*, **62**, e2022RG000781 (<https://doi.org/10.1029/2022RG000781>)

Brennan PV, Lok LB, Nicholls K and Corr H (2014) Phase-sensitive FMCW radar system for high-precision Antarctic ice shelf profile monitoring. *IET Radar, Sonar & Navigation.*, **8**(7), 776-786 (<https://doi.org/10.1049/iet-rsn.2013.0053>)

Brett GM, Irvin A, Rack W, Haas C, Langhorne PJ and Leonard GH (2020) Variability in the distribution of fast ice and the sub-ice platelet layer near McMurdo Ice Shelf. *J. Geophys. Res. Oceans.*, **125**, e2019JC015678 (<https://doi.org/10.1029/2019JC015678>)

Campbell AJ, Hulbe CL and Lee C-K (2018) Ice stream slowdown will drive long-term thinning of the Ross Ice Shelf, with or without ocean warming. *Geophys. Res. Lett.*, **45**, 201–206 (<https://doi.org/10.1002/2017GL075794>)

Carter SP and HA Fricker (2012) The Supply of Subglacial Meltwater to the Grounding Line of the Siple Coast, West Antarctica. *Annals of Glaciology.*, **53**, no. 60: 267–80 (<https://doi.org/10.3189/2012AoG60A119>)

Catania G, Hulbe C, Conway H, Scambos TA and Raymond CF (2012) Variability in the mass flux of the Ross ice streams, West Antarctica, over the last millennium. *J. Glaciol.*, **58**, 741–752 (<https://doi.org/10.3189/2012JoG11J219>)

Catania GA, TA Scambos H, Conway and CF Raymond (2006) Sequential stagnation of Kamb Ice Stream, West Antarctica, *Geophys. Res. Lett.*, **33**, L14502 ([doi:10.1029/2006GL026430](https://doi.org/10.1029/2006GL026430))

Das I and 11 others (2020) Multidecadal basal melt rates and structure of the Ross Ice Shelf, Antarctica, using airborne ice penetrating radar. *J. Geophys. Res: Earth Surface.*, **125**, e2019JF005241 (<https://doi.org/10.1029/2019JF005241>)

DeConto R and Pollard D (2016) Contribution of Antarctica to past and future sea-level rise. *Nature.*, **531**, 591–597 (<https://doi.org/10.1038/nature17145>)

Depoorter MA and 6 others (2013) Calving fluxes and basal melt rates of Antarctic ice shelves. *Nature.*, **502**(7469), 89–92 (<https://doi.org/10.1038/nature12567>)

Diener T, Sasgen I, Agosta C, Fürst JJ, Braun MH, Konrad H, Fettweis X (2021) Acceleration of Dynamic Ice Loss in Antarctica From Satellite Gravimetry. *Frontiers in Earth Science.*, **9** (<https://doi.org/10.3389/feart.2021.741789>)

Dupont TK and Alley RB (2005) Assessment of the importance of ice-shelf buttressing to ice-sheet flow. *Geophys. Res. Lett.*, **32**(4) (<https://doi.org/doi:10.1029/2004GL022024>)

Edwards TL and 83 others (2021) Projected land ice contributions to twenty-first-century sea level rise. *Nature.*, **593**, 74–82 (<https://doi.org/10.1038/s41586-021-03302-y>)

Fretwell P and 59 others (2013) Bedmap2: improved ice bed, surface and thickness datasets for Antarctica. *The Cryosphere.*, **7**, 375–393 (<https://doi.org/10.5194/tc-7-375-2013>)

Fricker HA, Popov S, Allison I and Young N (2001) Distribution of marine ice beneath the Amery Ice Shelf. *Geophys. Res. Lett.*, **28**, 2241–2244 (<https://doi.org/10.1029/2000GL012461>)

Gagliardini O, Zwinger T, Gillet-Chaulet F, Durand G, Favier L, de Fleurian B, Greve R, Malinen M, Martín C, Råback P, Ruokolainen J, Sacchettini M, Schäfer M, Seddik H and Thies J (2013) Capabilities and performance of Elmer/Ice, a new-generation ice sheet model. *Geosci. Model Dev.*, **6**(4), 1299–1318 (<https://doi.org/10.5194/gmd-6-1299-2013>)

Gardner AS, Schlegel NJ and Larour E (2023) Glacier Energy and Mass Balance (GEMB): a model of firn processes for cryosphere research. *Geosci. Model Dev.*, **16**, 2277–2302, (<https://doi.org/10.5194/gmd-16-2277-2023>)

Gardner AS, Fahnestock M and Scambos T (2022) MEaSURES ITS_LIVE Regional Glacier and Ice Sheet Surface Velocities, Version 1, NASA National Snow and Ice Data Center Distributed Active Archive Center [data set] (<https://doi.org/10.5067/6II6VW8LLWJ7>)

Gardner AS, Moholdt G, Scambos T, Fahnestock M, Ligtenberg S, van den Broeke M and Nilsson J (2018) Increased West Antarctic and unchanged East Antarctic ice discharge over the last 7 years. *The Cryosphere.*, **12**, 521–547 (<https://doi.org/10.5194/tc-12-521-2018>)

Greene CA, Gardner AS, Schlegel NJ and Fraser AD (2022) Antarctic calving loss rivals ice-shelf thinning. *Nature.*, **609**, 948–953 (<https://doi.org/10.1038/s41586-022-05037-w>)

Gudmundsson GH, Paolo FS, Adusumilli S and Fricker HA (2019) Instantaneous Antarctic ice-sheet mass loss driven by thinning ice shelves. *Geophys. Res. Lett.*, **46**, 13903–13909 (<https://doi.org/10.1029/2019GL085027>)

Gustafson CD and 6 others (2022) A dynamic saline groundwater system mapped beneath an Antarctic ice stream. *Science.*, **376**, 640–644 (DOI: 10.1126/science.abm3301)

Haran T, Klinger M, Bohlander, J Fahnestock M, Painter T and Scambos T (2018) updated 2019. MEaSUREs MODIS Mosaic of Antarctica 2013–2014 (MOA2014) Image Map, Version 1. [Ross Ice Shelf]. Boulder, Colorado USA. NASA National Snow and Ice Data Center Distributed Active Archive Center (<https://doi.org/10.5067/RNF17BP824UM>)

Hulbe C and Fahnestock M (2007) Century-scale discharge stagnation and reactivation of the Ross ice streams, West Antarctica. *J. Geophys. Res: Earth Surface.*, **112**(F3) (<https://doi.org/https://doi.org/10.1029/2006JF000603>)

Hulbe CL, Scambos TA, Youngberg T and Lamb AK (2008) Patterns of glacier response to disintegration of the Larsen B ice shelf, Antarctic Peninsula. *Global and Planetary Change.*, **63**(1), 1–8 (<https://doi.org/10.1016/j.gloplacha.2008.04.001>)

Jacobs SS, Helmer HH, Doake CSM, Jenkins A and Frolich RM (1992) Melting of ice shelves and the mass balance of Antarctica. *Journal of Glaciology.*, **38**(130), 375–387 (doi.org/10.3189/S0022143000002252)

Jacobs SS, Gordon AL and Ardai JL Jr (1979) Circulation and melting beneath the Ross Ice Shelf. *Science.*, **203**, 439–443 (doi:10.1126/science.203.4379.439)

Jacobs SS and CF Giulivi (2010) Large Multidecadal Salinity Trends near the Pacific–Antarctic Continental Margin. *J. Climate*, **23**, 4508–4524 (<https://doi.org/10.1175/2010JCLI3284.1>)

Jendersie S, Williams M, Langhorne PJ and Robertson R (2018) The density-driven winter intensification of the Ross Sea circulation. *J. Geophys. Res. Oceans.*, **123**, 7702–7724 (<https://doi.org/10.1029/2018JC013965>)

Lawrence JD and 15 others (2023) Crevasse refreezing and signatures of retreat observed at Kamb Ice Stream grounding zone. *Nat. Geosci.*, **16**, 238–243 (<https://doi.org/10.1038/s41561-023-01129-y>)

LeDoux CM, Hulbe C, Forbes MP, Scambos TA and Alley K (2017) Structural Provinces of the Ross Ice Shelf, Antarctica. *Annals of Glaciology.*, **58.**, no. 75 pt1 (2017): 88–98. (<https://doi.org/10.1017/aog.2017.24>)

Ligtenberg SRM, Helsen MM and van den Broeke MR (2011) An improved semi-empirical model for the densification of Antarctic firn. *The Cryosphere.*, **5**, 809-819 (<https://doi.org/10.5194/tc-5-809-2011>)

MacGregor JA, Anandakrishnan S, Catania GA and Winebrenner DP (2011) The Grounding Zone of the Ross Ice Shelf, West Antarctica, from Ice-Penetrating Radar. *Journal of Glaciology.*, **57**, no. 205: 917–28 (<https://doi.org/10.3189/002214311798043780>)

Malyarenko A, Robinson NJ, Williams MJM and Langhorne PJ (2019) A wedge mechanism for summer surface water inflow into the Ross ice shelf cavity. *J. Geophys. Res: Oceans.*, **124**, 1196–1214 (<https://doi.org/10.1029/2018JC014594>)

Marsh OJ and 6 others (2016) High basal melting forming a channel at the grounding line of Ross Ice Shelf, Antarctica. *Geophys. Res. Lett.*, **43**(1), 250-255 (<https://doi.org/10.1002/2015GL066612>)

Moholdt G, Padman L and Fricker HA (2014) Basal mass budget of Ross and Filchner-Ronne ice shelves, Antarctica, derived from Lagrangian analysis of ICESat altimetry. *J. Geophys. Res: Earth Surface.*, **119**(11), 2361-2380 (<https://doi.org/10.1002/2014jf003171>)

Morlighem, M (2022) MEaSURES BedMachine Antarctica, Version 3 [Data Set]. Boulder, Colorado USA. NASA National Snow and Ice Data Center Distributed Active Archive Center. (<https://doi.org/10.5067/FPSU0V1MWUB6>)

Morlighem, M and 36 others. 2020. Deep glacial troughs and stabilizing ridges unveiled beneath the margins of the Antarctic ice sheet. *Nature Geoscience.*, **13** (DOI: 10.1038/s41561-019-0510-8)

Mouginot J, Rignot E and Scheuchl B (2019). MEaSURES Phase-Based Antarctica Ice Velocity Map. (NSIDC-0754, Version 1) [Data Set]. Boulder, Colorado USA. NASA National Snow and Ice Data Center Distributed Active Archive Center. (<https://doi.org/10.5067/PZ3NJ5RXXRH10>)

Mouginot J, Rignot E, Scheuchl B and Millan R (2017) Comprehensive annual ice sheet velocity mapping using Landsat-8, Sentinel-1, and RADARSAT-2 data. *Remote Sensing.*, **9**(4), 364 (<https://doi.org/10.3390/rs9040364>)

Neal, CS (1979) The Dynamics of the Ross Ice Shelf Revealed by Radio Echo-Sounding. *Journal of Glaciology.*, **24**, no. 90: 295-307 (doi:10.3189/S0022143000014817)

Nicholls K, Corr H, Stewart C, Lok L, Brennan P and Vaughan D (2015) A ground-based radar for measuring vertical strain rates and time-varying basal melt rates in ice sheets and shelves. *Journal of Glaciology.*, **61**(230), 1079-1087 (doi:10.3189/2015JoG15J073)

Parkinson C (2019) A 40-y record reveals gradual Antarctic sea ice increases followed by decreases at rates far exceeding the rates seen in the Arctic. *Proc. Natl. Acad. Sci.* **116** (29) 14414-14423 (<https://doi.org/10.1073/pnas.1906556111>)

Paolo, F. S and 6 others (2023) Widespread slowdown in thinning rates of West Antarctic ice shelves, *The Cryosphere.*, **17**, 3409–3433 (<https://doi.org/10.5194/tc-17-3409-2023>)

Paolo FS, Fricker HA and Padman L (2015) Volume loss from Antarctic ice shelves is accelerating. *Science.*, **348**(6232), 327-331 (DOI: 10.1126/science.aaa0940)

Price S, Bindshadler R, Hulbe CL and Joughin IR (2001) Post-stagnation behavior in the upstream regions of Ice Stream C, West Antarctica. *Journal of Glaciology.*, **47**, 283-294 (<https://doi.org/10.3189/172756501781832232>)

Rack W and Rott H (2004) Pattern of retreat and disintegration of the Larsen B ice shelf, Antarctic Peninsula. *Annals of Glaciology.*, **39**, 505-510 (<https://doi.org/10.3189/172756404781814005>)

Retzlaff R and Bentley C.R (1993) Timing of stagnation of Ice Stream C, West Antarctica, from short-pulse radar studies of buried surface crevasses. *Journal of Glaciology.*, **39**(133), 553-561 (<https://doi.org/10.3189/S0022143000016440>)

Rignot E, Mouginot J, Scheuchl B, van den Broeke M, van Wessem MJ and Morlighem M (2019) Four decades of Antarctic Ice Sheet mass balance from 1979–2017. *Proceedings of the National Academy of Sciences.*, **116**(4), 1095-1103 (<https://doi.org/10.1073/pnas.1812883116>)

Rignot E, Mouginot J and Scheuchl B (2017) MEaSURES InSAR-Based Antarctica Ice Velocity Map, Version 2 [Data Set]. Boulder, Colorado USA. NASA National Snow and Ice Data Center Distributed Active Archive Center (<https://doi.org/10.5067/D7GK8F5J8M8R>)

Rignot E, Jacobs S, Mouginot J and Scheuchl B (2013) Ice-Shelf Melting Around Antarctica. *Science.*, **341**(6143), 266-270 (<https://doi.org/10.1126/science.1235798>)

Rignot E, Mouginot J and Scheuchl B (2011) Ice flow of the Antarctic ice sheet. *Science.*, **333**(6048), 1427-1430 (DOI: 10.1126/science.1208336)

Rignot E, Casassa G, Gogineni P, Krabill, W, Rivera A and Thomas R (2004) Accelerated ice discharge from the Antarctic Peninsula following the collapse of Larsen B ice shelf. *Geophys. Res. Lett.*, **31**(18) (<https://doi.org/10.1029/2004gl020697>)

Rott H, Rack W, Skvarca P and Angelis HD (2002) Northern Larsen Ice Shelf, Antarctica: further retreat after collapse. *Annals of Glaciology.*, **34**, 277-282 (<https://doi.org/10.3189/172756402781817716>)

Ryan MR (2016) Characteristics of the Ross and Southern McMurdo ice shelves as revealed from ground-based radar surveys: a thesis submitted in partial fulfilment of the requirements for the degree of Master of Science in Environmental Science, Gateway Antarctica, University of Canterbury (<http://dx.doi.org/10.26021/6284>)

Seroussi H and 48 others (2023) Insights into the vulnerability of Antarctic glaciers from the ISMIP6 ice sheet model ensemble and associated uncertainty. *The Cryosphere.*, **17**, 5197–5217 (<https://doi.org/10.5194/tc-17-5197-2023>, 2023)

Siegfried MR, Fricker HA, Carter SP and Tulaczyk S (2016) Episodic ice velocity fluctuations triggered by a subglacial flood in West Antarctica. *Geophys. Res. Lett.*, **43**, 2640–2648, (doi:10.1002/2016GL067758)

Smith B and others (2020) Pervasive ice sheet mass loss reflects competing ocean and atmosphere processes. *Science.*, **368**, 1239-1242 (DOI:10.1126/science.aaz5845)

Stewart CL (2018) Ice-ocean interactions beneath the north-western Ross Ice Shelf, Antarctica [Apollo - University of Cambridge Repository] (<https://doi.org/10.17863/CAM.21483>)

Stewart CL, Christoffersen P, Nicholls KW, Williams MJM and Dowdeswell JA (2019) Basal melting of Ross Ice Shelf from solar heat absorption in an ice-front polynya. *Nature Geoscience.*, **12**(6), 435-440 (<https://doi.org/10.1038/s41561-019-0356-0>)

Stevens C and 6 others (2020) Ocean mixing and heat transport processes observed under the Ross Ice Shelf control its basal melting. *Proceedings of the National Academy of Sciences.*, **117**(29), 16799-16804 (<https://doi.org/10.1073/pnas.1910760117>)

Tankersley MD, Horgan HJ, Siddoway CS, Caratori Tontini F and Tinto KJ (2022) Basement topography and sediment thickness beneath Antarctica's Ross ice shelf. *Geophys. Res. Lett.*, **49**, e2021GL097371 (<https://doi.org/10.1029/2021GL097371>)

Tinto KJ and others (2019) Ross Ice Shelf response to climate driven by the tectonic imprint on seafloor bathymetry. *Nature Geoscience.*, **12**(6), 441-449 (<https://doi.org/10.1038/s41561-019-0370-2>)

van der Wel N, Christoffersen P and Bougamont M (2013) The influence of subglacial hydrology on the flow of Kamb Ice Stream, West Antarctica, *J. Geophys. Res. Earth Surf.*, **118**, 97–110 (doi:10.1029/2012JF002570)

Vaňková I and Nicholls KW (2022) Ocean variability beneath the Filchner-Ronne Ice Shelf inferred from basal melt rate time series. *J. Geophys. Res: Oceans.*, **127**, e2022JC018879 (<https://doi.org/10.1029/2022JC018879>)

Vaňková I, Nicholls KW and Corr HFJ (2021) The nature of ice intermittently accreted at the base of Ronne Ice Shelf, Antarctica, assessed using phase-sensitive radar. *J. Geophys. Res: Oceans.*, **126**, e2021JC017290 (<https://doi.org/10.1029/2021JC017290>)

van der Wel N, Christoffersen P and Bougamont M (2013) The influence of subglacial hydrology on the flow of Kamb Ice Stream, West Antarctica. *J. Geophys. Res: Earth Surf.*, **118**, 97–110 (doi:10.1029/2012JF002570)

Verboncoeur H and 7 others (2024) Multi-decadal evolution of Crary Ice Rise region, West Antarctica, amid modern ice-stream deceleration. *Journal of Glaciology.*, **71**:e3 (doi:10.1017/jog.2024.79)

Washam P and 14 others (2023) Direct observations of melting, freezing, and ocean circulation in an ice shelf basal crevasse. *Sci. Adv.*, **9**, eadi7638 (DOI:10.1126/sciadv.adi7638)

Wild CT and 18 others (2024) Rift propagation signals the last act of the Thwaites Eastern Ice Shelf despite low basal melt rates. *Journal of Glaciology.*, **70** (doi:10.1017/jog.2024.64)

Whiteford A, Horgan HJ, Leong WJ and Forbes M (2022) Melting and refreezing in an ice shelf basal channel at the grounding line of the Kamb Ice Stream, West Antarctica. *J. Geophys. Res: Earth Surf.*, **127**, e2021JF006532 (<https://doi.org/10.1029/2021JF006532>)

Winberry JP, Anandakrishnan S, Alley RB, Wiens DA, and Pratt MJ (2014) Tidal pacing, skipped slips, and the slowdown of Whillans Ice Stream, Antarctica. *Journal of Glaciology.*, **60**, 222–807 (<https://doi.org/10.3189/2014JoG14J038>)

Xie C, Zhang Z, Chen Y, Wang C and Zhou M (2024) The response of Ross Sea shelf water properties to enhanced Amundsen Sea ice shelf melting. *J. Geophys. Res: Oceans.*, **129**, e2024JC020919 (<https://doi.org/10.1029/2024JC020919>)

Zeising O and 6 others (2024) Extreme melting at Greenland's largest floating ice tongue, *The Cryosphere.*, **18**, 1333–1357 (<https://doi.org/10.5194/tc-18-1333-2024>)

Zeising O, Steinhage D, Nicholls KW, Corr HFJ, Stewart CL and Humbert A (2022) Basal melt of the southern Filchner Ice Shelf, Antarctica. *The Cryosphere.*, **16**, 1469–1482 (<https://doi.org/10.5194/tc-16-1469-2022>)

Zotikov IA, Zagorodnov VS and Raikovskiy JV (1980) Core Drilling Through the Ross Ice Shelf (Antarctica) Confirmed Basal Freezing. *Science.*, **207**, Issue 4438, pp. 1463-1465 (DOI: 10.1126/science.207.4438.1463)

Fig. 1. ApRES site locations S1-S32 across the RIS plotted over the Bedmap2 ice thickness (Fretwell and others, 2013) and the MODIS Mosaic of Antarctica (Haran and others, 2019) with streaklines modified after LeDoux and others (2017). The heavy white lines outline the flow band from Liv Glacier to the HWD2 borehole, where a ~60 m thick layer of accreted basal ice was observed. All cavity drill hole access points are shown by black crosses - KIS1, KIS2, KIS3, J9, WIS (also known as WISSARD), HWD2 & CH-1,2. The spatial distributions of previous ApRES assessments on the RIS are shown by cyan lines. The U.S. South Pole Traverse (SPoT) and New Zealand Siple Coast Traverse (SCT) routes are identified. **Upper right inset:** Glacial basins feeding the Ross Ice Shelf (RIS) from the West Antarctic Ice Sheet (WAIS – light grey), and East Antarctic Ice Sheet (EAIS – dark grey), **Lower left inset:** Ice shelf melting Mode 1 driven by High Salinity Shelf Water (HSSW), Mode 2 by Circumpolar Deep Water/modified-Circumpolar Deep Water (mCDW) (this mode is not consistently observed in the Ross cavity), and Mode 3 by Antarctic Surface Water (AASW) at the ice shelf front.

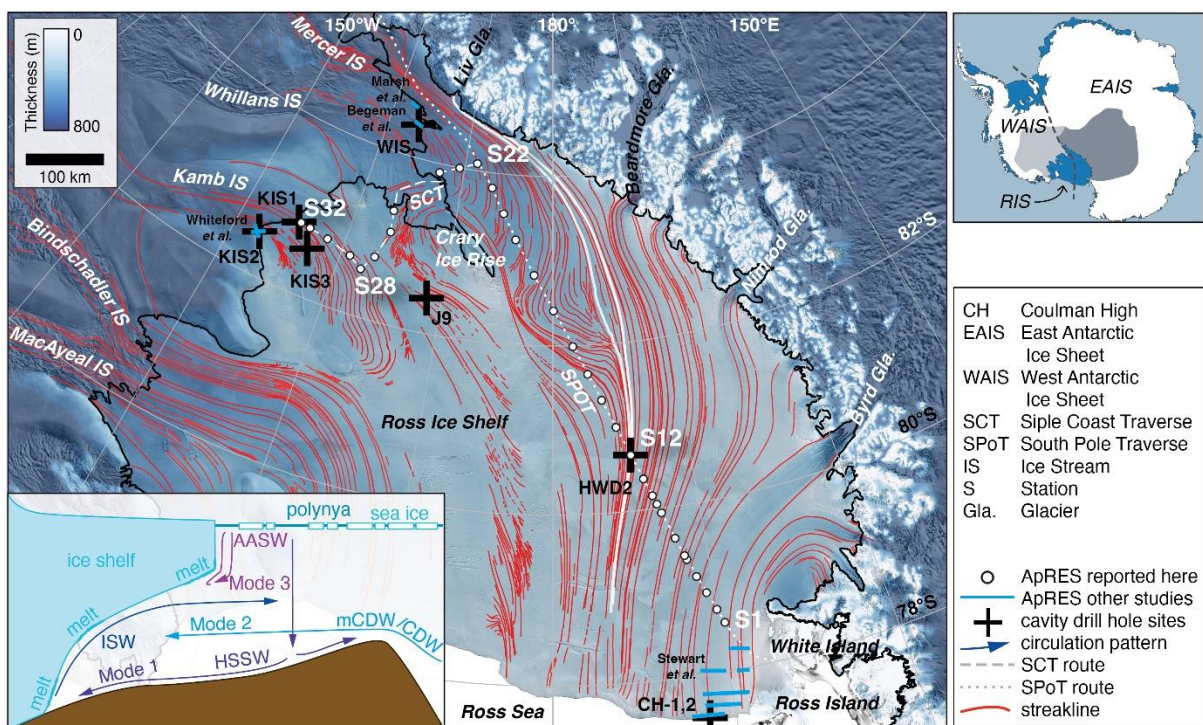


Fig. 2. (a) Map of ApRES measurement sites S1-S32, respective melt zones, colour-coded basal reflection categories and typical ApRES waveforms for different reflection strengths. Reflection coefficients are shown as contour lines adapted from Neal (1979). Contours are at 10 dB intervals, with open shading greater than 0 dB, and heavy shading less than -20 dB. Subset of Ross Ice Shelf drilling sites are shown by black crosses **(b)** ApRES site variation of the basal peak reflection amplitude relative to the near basal internal reflection (dB). All ApRES measurements with the same attenuation settings at each site have been included, some sites have multiple data points per year, the grey line connects the means of each site **(c)** airborne-derived signal power, a relative number with 0 dB being some arbitrary value that is consistent as long as there are no significant changes with processing (Tinto and others, 2019); values shown are the mean of all airborne survey values and standard deviations available within a 5 km radius of each ApRES site (21 out of 32 sites).

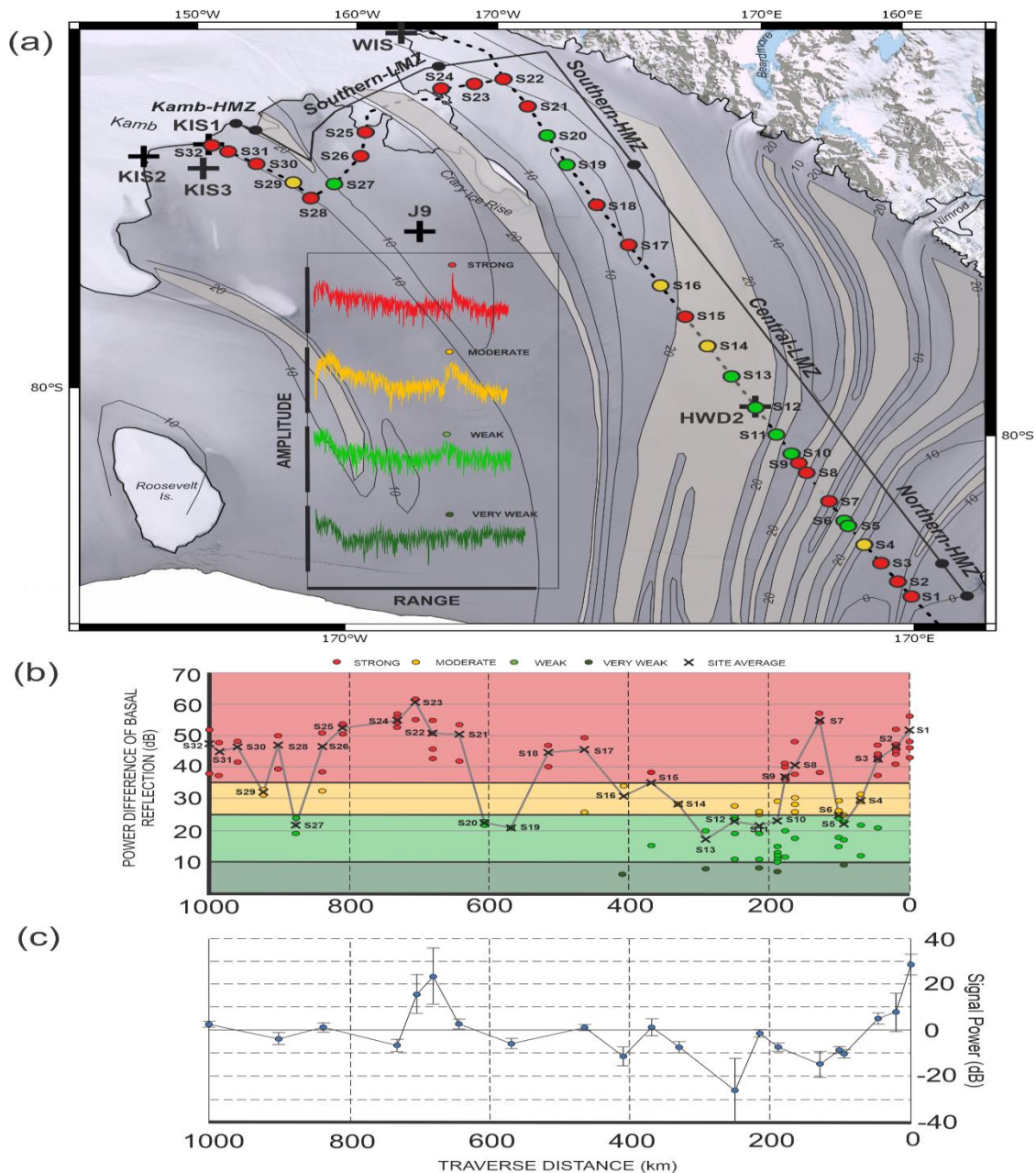


Fig. 3. (a) ApRES basal melt rates (black dots) and melt zones, strain rates (blue triangles), with errors, the marker obscures small error bars. Zero lines are shown for each dataset, the dotted black line is the Ross Ice Shelf ApRES-derived mean melt rate (b) ApRES melt rate plotted with comparable satellite and airborne investigations, melt rate values from Das and others (2020) were not available for all ApRES sites, satellite data sets show errors except for Paolo and others (2023) which displays the standard deviation as errors were not available for the provided mean basal melt rate (c) RIS-wide spatial distribution of basal melt rate from Paolo and others (2023) (d) Adusumilli and others (2020) and, (e) Das and others (2020) with ApRES transect for reference, and (f) displays the spatial distribution of ApRES-derived basal melt with site symbols scaled for the magnitude of melt. The background image in c-f is the MODIS Mosaic of Antarctica (Haran and others. 2019).

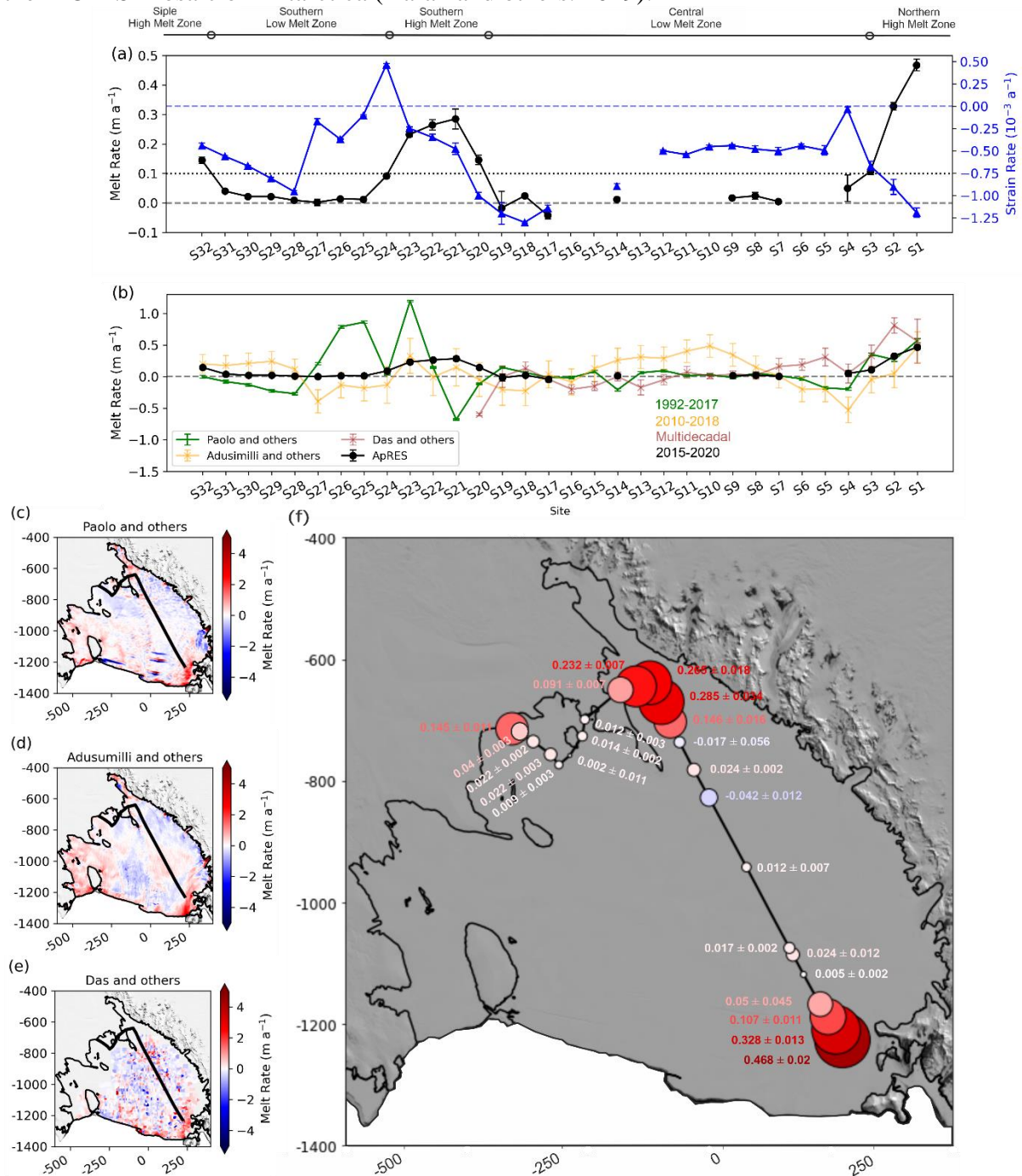


Fig. 4. (a) Multi-year repeats of measurements across the Northern High Melt Zone (S1-S3 + S4 for reference) (b) mean of all available measurements at each site plotted with estimates of the Jan 2013-Jan 2014 mean melt rate from Stewart (2018) at transect sites a5, b7, c7, d6, e7 toward the ice shelf front.

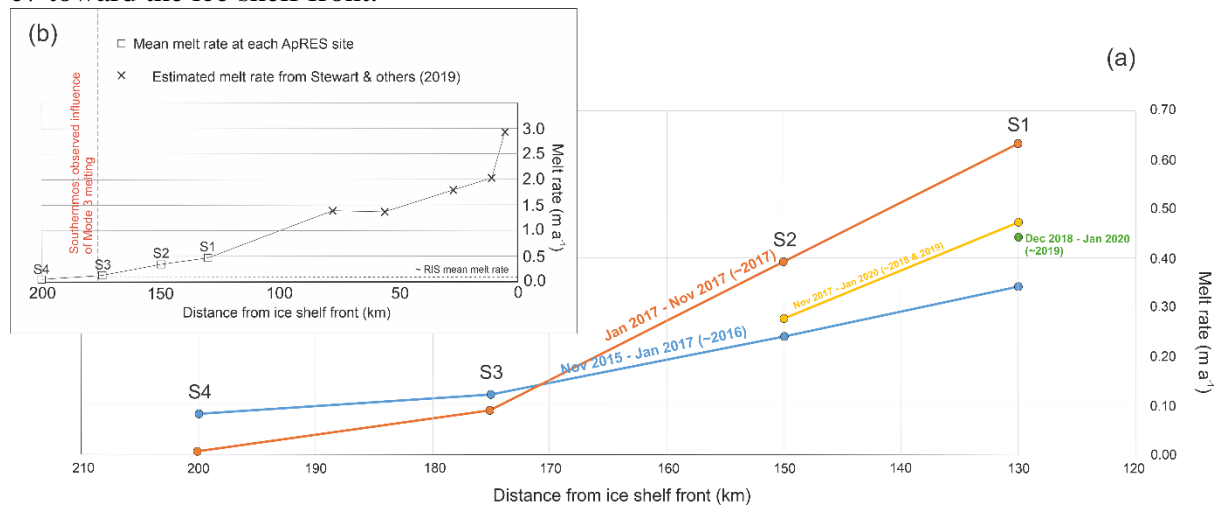


Fig. 5. Correlation between ApRES and satellite observed (Alley and others, 2018; Rignot and others, 2017) vertical strain rates (\square). The orange line represents the 1:1 line. Satellite derived \square uncertainty represents the standard deviation of the 3 x 3 km box around the ApRES site.

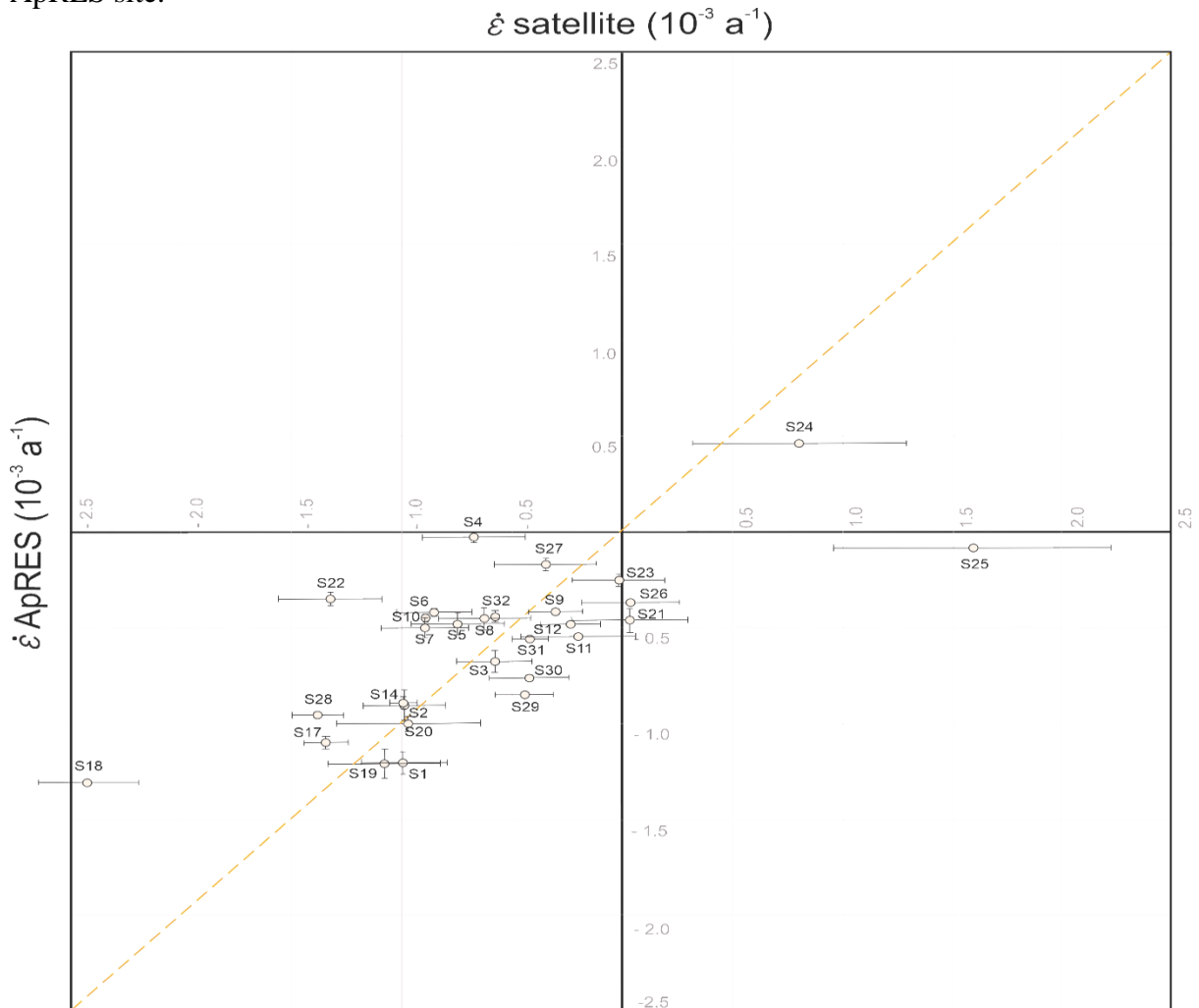


Fig. 6. Overview of oceanographic observations with water masses displayed as High Salinity Shelf Water (HSSW), Ice Shelf Water (ISW), ISW+HSSW, Antarctic Surface Water (AASW), and mix which could not be defined as a particular water mass but had temperatures (T) associated with HSSW and salinity (S) associated with mCDW. ApRES reflection strengths and the glaciological regime along the ApRES transect across the Ross Ice Shelf are also summarised. Roosevelt Island, Ross Island, the Crary Ice Rise, Coulman High (CH) and Discovery Deep (DD) are also identified.

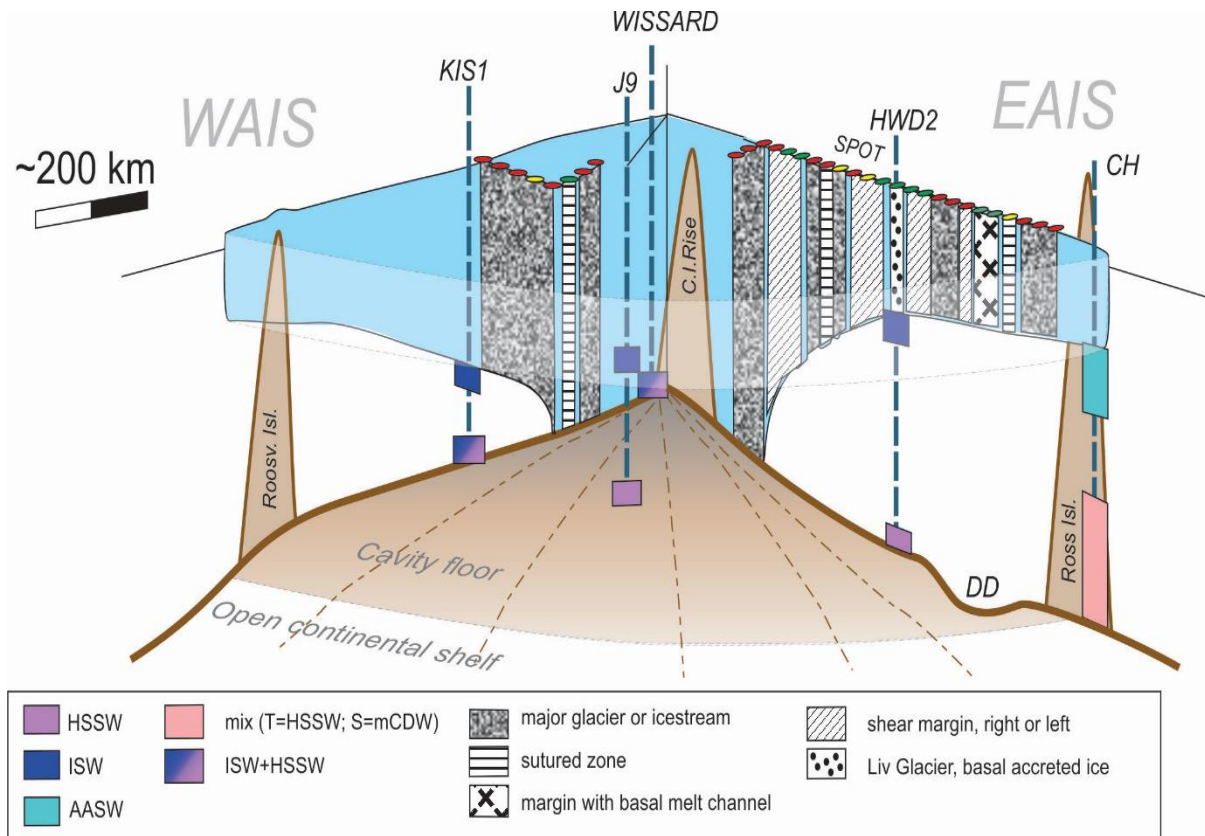


Table 1. Ice shelf thickness (firm corrected) with comparisons to commonly used satellite altimetry-derived thickness products, reflection strength, basal melt rate and errors, vertical strain rate (\square) and errors. Sites marked with a * show the averaged basal melt/strain rates from the available measurements up to four years, remaining data are rates as determined between austral summer 2018 and 2019. Reported reflection strength and thickness are the mean of all data available at each site, reflection strength mean values are calculated only using measurements with the same attenuation settings.

Site	ApRES Thickness minus (<i>BEDMAP2</i> : <i>BedMachine V3</i>) m	Reflection Strength	Melt Rate (error) m a^{-1}	\square (error) 10^{-3} a^{-1}	Flow band
S1*	329.1 (21.5 : 9.2)	Strong	0.468 (0.020)	-1.19 (0.0529)	Byrd Glacier (middle margin)
S2*	362.1 (31.1 : 28.6)	Strong	0.328 (0.013)	-0.904 (0.0844)	Byrd Glacier (middle margin)
S3*	367.3 (21.3 : 13.2)	Strong	0.107 (0.011)	-0.670 (0.0553)	Byrd Glacier (middle margin)
S4*	410.4 (44.4 : 28.6)	Moderate	0.05 (0.045)	-0.336 (0.0262)	Grazzini Bay coastline (sutured margins)
S5*	375.3 (14.3 : 0.2)	Weak	-	-0.493 (0.0525)	Nimrod Glacier (shear margin / basal melt channel)
S6*	388.9 (30.9 : 19.4)	Weak	-	-0.442 (0.0193)	Nimrod Glacier (shear margin / basal melt channel)
S7*	386.2 (26.2 : 47.7)	Strong	0.005 (0.002)	-0.503 (0.0423)	Lennox-King Glacier (true left margin)
S8*	351.8 (-1.2 : 18.0)	Strong	0.024 (0.012)	-0.479 (0.0346)	Beardmore Glacier (true left margin to middle margin)
S9	342.0 (-6.0 : 6.1)	Strong	0.017 (0.002)	-0.440 (0.0110)	Beardmore Glacier (middle margin)
S10	322.6 (-20.4 : -8.8)	Weak	-	-0.453 (0.0194)	Beardmore Glacier (true right margin shear band)
S11	329.5 (-24.5 : -21.1)	Weak	-	-0.541 (0.0115)	Sutured margins, Canyon Glacier (true right margin)
S12	328.6 (-16.4 : 15.2) HWD2 borehole (367.5) approx. 2 km separation	Weak	-	-0.498 (0.00841)	Liv Glacier (ice-filled basal crevasses)
S13	317.9 (-30.1 : -1.2)	Weak	-	-	CIR (true left margin, shear & transverse rifts - same trajectory as S15)
S14	348.6 (-17.4 : 8.3)	Moderate	0.012 (0.007)	-0.895 (0.0303)	CIR (true left margin, transverse rifts)

S15	379.4 (14.4 : 34.2)	Strong	-	-	CIR (true left margin, shear & transverse rifts - same trajectory as S13)
S16	393.8 (-12.2 : 25.4)	Moderate	-	-	Mercer Ice Stream (complicated folding history)
S17	468.8 (6.8 : 12.0)	Strong	-0.042 (0.012)	-1.14 (0.0336)	MacDonald Nunataks / south of MacD N
S18	503.2 (11.2 : 6.9)	Strong	0.024 (0.002)	-1.30 (0.00601)	Leverett Glacier
S19	565.8 (-0.2 : 9.5)	Weak	-0.017 (0.056)	-1.20 (0.122)	Mercer Ice Stream (true left margin, deformation history)
S20	601.8 (-1.2 : 16.2)	Weak	0.146 (0.016)	-1.00 (0.0355)	Mercer Ice Stream (true left margin, deformation history)
S21	641.4 (10.4 : -2.8)	Strong	0.285 (0.034)	-0.476 (0.0648)	Mercer Ice Stream
S22	680.8 (22.8 : 16.3)	Strong	0.265 (0.018)	-0.348 (0.0342)	WIS
S23	686.6 (24.6 : 21.1)	Strong	0.232 (0.007)	-0.247 (0.0151)	WIS
S24	695.6 (16.6 : 23.5)	Strong	0.091 (0.007)	0.462 (0.0152)	WIS
S25	571.1 (16.1 : 20.5)	Strong	0.012 (0.003)	-0.103 (0.00854)	WIS
S26	502.8 (5.8 : 23.0)	Strong	0.014 (0.002)	-0.368 (0.00513)	WIS
S27	495.6 (35.6 : 23.4)	Weak	0.002 (0.011)	-0.171 (0.0328)	Sutured margins, WIS and KIS
S28	466.9 (10.9 : 6.0)	Strong	0.009 (0.003)	-0.955 (0.0108)	KIS
S29	476.5 (8.5 : -0.1)	Moderate	0.022 (0.003)	-0.807 (0.0108)	KIS
S30	526.3 (10.3 : -9.0)	Strong	0.022 (0.002)	-0.668 (0.00752)	KIS
S31	574.5 (12.5 : 14.8)	Strong	0.040 (0.003)	-0.560 (0.00990)	KIS
S32	576.0 (21.0 : 18.1) KIS1 borehole (583.4) approx. 3 km separation	Strong	0.145 (0.011)	-0.440 (0.0286)	KIS

Table 2. Key characteristics and relevant auxiliary data set information for ApRES basal melt and satellite/airborne comparison products used for this study.

Product	Method and timespan	SMB; firn	Ice velocity	Grid for basal melt
ApRES (this study)	Surface-based phase-sensitive radar – Langrangian (S1-S12 2016 through 2019; S13-S32 2019)	N/A; BedMachine V3 ¹	N/A	Point measurement
A2020	Altimetry - Langrangian (2010-2018)	MERRA-2 ² /M2R12K ³ ; ⁴ Community Firn Model/ ⁵ GSFC-FDMv0	Landsat-7 & 8 ⁷	500 m
P2023	Altimetry – Eulerian (1992-2017)	GEMB ⁶	Multi-mission blended products ^{7,8,9}	3000 m
D2020	Airborne radar – Langrangian (Multidecadal and variable ~10-60 years)	N/A	MEaSURES v2 ¹⁰ /ELMER/Ice ¹¹	Airborne radar transects at 10-30 km spacing - bivariate spline ~ 10 km grid

Surface Mass Balance and Firn processes:

¹Morlighem (2022); ²Gelaro and others (2017)/³Smith and others (2020); ⁴Stevens and others (2020)/⁵Smith and others (2020); ⁶Gardner and others (2023)

Ice velocities:

⁷Gardner and others (2018); ⁸Mouginot and others (2019)/⁹Gardner and others (2022); ¹⁰Rignot and others (2017); ¹¹Gagliardini and others (2013)